

Turbulence of the Solar Wind

Studies of the Solar Wind Using the ACE and Helios Spacecraft

Bejamin T. MacBride
Department of Physics
University of New Hampshire
Durham, NH 03824

May 16, 2007

Abstract

The solar wind is a supersonic flow of plasma emanating from the sun and traveling through the interplanetary medium to the outermost reaches of the heliosphere. The solar wind experiences in situ magnetohydrodynamic (MHD) turbulence as it expands from its source. This thesis has two components with the common theme of turbulence: one examines the heating from the turbulent cascade at 1 AU, and the other studies the spatial evolution of the interplanetary spectrum of solar wind turbulence.

Models based on turbulence provide enough energy to account for the heating of the solar wind relative to an adiabatic expansion that has been observed by the Voyager spacecraft [53]. In this work we employ Kolmogorov's expression for the rate of energy cascade per unit mass based on the third-order structure function of velocity fluctuations in hydrodynamic turbulence. The solar wind, however, is MHD and its turbulence is anisotropic. *Politano and Pouquet* [50, 51] have derived an expression - valid in anisotropic situations - for the cascade rate based on the third moment of fluctuations in MHD turbulence. We perform an analysis of the third moment derived by Politano and Pouquet and use 8 years of combined magnetic field and plasma measurements from the Advanced Composition Explorer to compute the cascade rate of the turbulence in the solar wind. We find the energy cascade inferred from traditional methods using the power spectrum of fluctuations is higher than what is shown from the local temperature gradient of the solar wind, and that the third-order structure function formalism provides an accurate prediction of the energy cascade.

By analyzing the small scale properties of the turbulence it is possible to come to an understanding of the dynamics of the energy as it moves through the inertial range and is dissipated to heat the background plasma. We construct a database with 387 intervals of Helios 1 observations at spacecraft frame frequencies ranging from $5 - 70 \times 10^{-3}$ Hz. We find the variance anisotropy scales with both plasma beta and the amplitude of the power spectrum of magnetic fluctuations. We also find the energy to be nearly equally distributed between field-aligned and perpendicular wave vectors. These results are derived in the region between 0.3 and 1.0 AU and show no dependence on heliocentric distance. This confirms that the results of *Leamon et al.* [31], *Smith et al.* [61], and *Hamilton et al.* [22] in the near-earth atmosphere at 1 AU hold true inside the orbit of Mercury, which implies the turbulence of the solar wind is fully developed by the time it reaches 0.3 AU.

Contents

1	Introduction	2
1.1	Solar Wind Acceleration	2
1.2	Structured Solar Wind	3
1.3	Solar Cycle	4
1.4	Spacecraft Missions	5
2	Solar Wind Structure and Fluctuations	9
2.1	Parker's Model of the Solar Wind	9
2.2	Interplanetary Magnetic Field	12
2.3	Plasma Waves in the Solar Wind	14
2.4	Wave Vectors in the Solar Wind	16
2.5	Heating of the Solar Wind	17
3	Solar Wind Turbulence	18
3.1	Interplanetary Spectrum	18
3.2	Energy-Containing Range	18
3.3	Inertial Range	18
3.4	Dissipation Range	20
3.5	Published Papers	20
4	Third Moment of Fluctuations in the Solar Wind	21
4.1	Introduction	21
4.2	Theory	22
4.2.1	Structure Function Formalism	23
4.3	Analysis	24
4.3.1	All Data	25
4.3.2	High and Low Wind Speed	28
4.3.3	Minority Components	31
4.3.4	Yearly Analysis	34
4.4	Summary	36
4.5	Detrending and Stationarity	36
4.6	Code Testing	37
5	Turbulence of the Inner Heliosphere	38
5.1	Anisotropic Turbulence in the Solar Wind	38
5.2	Helios Analysis	39
5.3	Magnetic Variance of the Inner Heliosphere	40
5.4	Spatial Evolution of the Power Spectral Index	42

5.5	Wave Vector Anisotropy of the Inner Heliosphere	43
5.6	Conclusion	46
6	Parting Remarks	48

Acknowledgements:

This work would not have been possible without the help of a supporting cast. First and foremost to the work presented in this thesis is the help provided by Professor Chuck Smith. Professor Smith has positively influenced my professional and academic career in a way I didn't think to be possible. He showed infinite patience and pedagogical abilities as he took me from the level of having zero programming experience and a rudimentary understanding of outer space to the point where I was able to present my work to and become engaged in conversations with leading space physicists at professional conferences. I owe a great deal of any success I may stumble upon to the years of support and guidance Professor Smith has given me.

As an educational institution, the University of New Hampshire has been very kind to me. From the first day I arrived on campus, the Physics Department has always treated me with a great deal of kindness and respect and I have found the academic environment in Demeritt Hall to be intellectually engaging and stimulating. I have been treated to the great teachings of Professors Calarco, Chupp, Echt, Harper, Holtrop, Meredith, and Ryan and I will take all that they have taught me into my years of graduate school. I would also like to thank my classmates Mike Antosh, Don Carlson, Jason Carrol, Jason Conwell, Kevin Godin, Andrew Gustafson, and Will Morrison for helping me to endure the homework sets and exams that accompany a degree in physics.

I would like to thank Professor Miriam Forman of the State University of New York at Stonybrook for her continual advice and guidance on solar wind turbulence theory. Professor Bernie Vasquez from the Space Science Center at UNH was also very helpful to me with the insight he provided on the heating and acceleration of the solar wind.

On a personal note, I would like to thank the lady I love, Hannah Varn, for being my companion in life. You never cease to amaze me with all that you do with your life.

Chapter 1

Introduction

The solar wind is a plasma that is an expansion of the sun's corona through the heliosphere at a supersonic rate until it reaches the termination shock where it slows down to a subsonic flow as it interacts with the heliopause, heliosheath, and the local interstellar medium. There exist fundamental questions that to this day remain unanswered by all the spacecraft observation and research in the field of solar wind studies. These questions are: where does the solar wind come from, and what is the source of its acceleration? The questions are so basic and simple, yet the answers have proven to be elusively complex.

The first predictions for the existence of a solar wind were made by Ludwig Biermann [7]. Biermann's prediction of a solar wind came from his study of comet tails. At the time of his research, the tails of comets were believed to be a result of electromagnetic radiation pressure alone. Biermann observed long cometary tails that weren't always pointed exactly radially away from the sun. He argued that these long tails could not be produced by radiation pressure alone. This radiation pressure must be coupled with another massive particle flux originating at the sun. He believed the lighter dust tails in comets are produced by electromagnetic radiation, but that the more massive tail region is produced by corpuscular radiation.

In 1957 Chapman [11] developed a static, subsonic model of the solar wind, but this model predicted ion densities and temperatures at the vicinity of earth that were too high. Eugene Parker [45, 46] argued against the static model of the solar wind and provided a model that predicts a supersonic flow of plasma extending throughout the heliosphere. His model assumes the pressure gradient in the solar atmosphere is such that particles are accelerated as they stream outwards from the sun until they reach a supersonic flow speed. Parker's supersonic solar wind prediction has been validated by in situ observations of the solar wind [44]. Parker's 1958 paper "Dynamics of the Interplanetary Gas and Magnetic Fields" was groundbreaking and is the foundation for modern solar wind research.

This paper is broken into 5 Chapters which give a description of solar wind properties and a particular focus on the turbulence of the solar wind.

1.1 Solar Wind Acceleration

The core of the sun is a nuclear reactor in which hydrogen nuclei are compounded together in the process known as nuclear fusion to create helium and excess (heat) energy. The heat energy produced in the core makes its way first through the radiative zone of the solar interior by the process of diffusive radiation. As the heat expands towards the edges of

the radiative zone it cools down and it becomes more efficient to transfer heat by means of convection and so convective cells develop and transfer heat through the convective zone. Above the convection zone lies the layer of the sun we refer to as the surface of the sun, or the photosphere. The photosphere is the layer of the sun that emits light, and is the reason we refer to this region as the solar surface. The photosphere has a temperature of approximately 5800 K. Above the photosphere is a region that has been labeled the chromosphere. When the bright photosphere is blotted out by either a solar eclipse or with a coronagraph, the chromosphere can be seen as the red-colored region just above the photosphere. The red color gives the chromosphere its name (*chroma* = Greek for color). The regions of the sun inside the chromosphere demonstrate a decrease in temperature with increasing distance from the core of the sun. However, the chromosphere, which is further from the core of the sun than the photosphere, has a higher average temperature than the photosphere. The corona is the solar atmosphere and lies above the chromosphere. This is the outermost layer of the sun and the solar wind is an extension of the corona into the interplanetary medium. Like the chromosphere, the corona can only be seen during a solar eclipse or with special optical instruments because of its dimness in comparison to the photosphere. The corona is even hotter than the chromosphere and exhibits an average temperature of approximately 10^6 K, more than a factor of 150 times as hot as the photosphere.

The temperature of the sun is the highest at its core and it decreases steadily as the heat is transported away from the core until it reaches the photosphere. Between the photosphere and the corona, the temperature of the sun increases from approximately six thousand to one million Kelvin. There are several theories for the source of this heating, but to this day none has been proven. The heat energy at the base of the corona is transferred to kinetic energy as the solar wind accelerates. The solar wind is accelerated to typical velocities ranging from 250-800 km/s (see Sections 1.2 and 2.1).

1.2 Structured Solar Wind

Observations show the solar wind exhibits two distinct flow speeds: fast and slow. The solar wind is highly structured at solar minimum typically with high wind sources at high latitudes and low wind sources at low latitudes. The degree of order and coherence of the solar wind is strongly correlated with the solar cycle (see Section 1.3). The slow velocity mode is characterized by a speed range of 250 – 400 km/s and the fast mode usually has speeds between from 400 – 800 km/s. The origin and unique properties and characteristics of the two types of wind have led physicists to treat them as two separate entities.

Studies have shown that the fast solar wind originates from coronal holes [69, 27]. Coronal holes are associated with open magnetic field lines that allow the solar wind to flow at a faster rate into the heliosphere. The fast solar wind has an average proton density of approximately three protons per cubic centimeter at 1 AU [56] and has approximately a four percent helium abundance. The typical proton temperature in the fast stream wind is 2.3×10^5 K and the electron temperature is 1×10^5 K [56].

The slow solar wind is believed to originate from multiple regions in the corona. Some of these sources include the boundaries between coronal holes and helmet streamers, plasma sheets near the cusps of streamers, small coronal holes, and active regions [12]. Helmet streamers in the corona are regions of closed magnetic field lines that form loops on the surface of the sun. The average proton density of the slow wind at a location of 1 AU from the sun is approximately 10.7 protons per cubic centimeter [56]. The slow solar wind is

more affected by the solar cycle than the fast solar wind. During solar minimum conditions the slow wind usually originates near the heliomagnetic equator and has a variable helium abundance. The electrons in the slow wind have average temperatures of 1.3×10^5 K and the protons in the slow solar wind have an average temperature of 3.4×10^4 K, which is nearly a factor of ten lower than the protons in the fast solar wind.

The location of the critical point (discussed in Section 2.1) in relation to where the solar wind receives the majority of its heating is an important factor in determining the nature of the solar wind [12]. In fact, it determines whether the flow is fast or slow. If the majority of the heating occurs below the critical point, when the solar wind is still subsonic and near the sun, then the plasma expands and the increase in energy provided by the heating is balanced by the mass flux and density increase as the wind draws in more particles and thus more mass from the corona and this limits the overall speed of the flow. On the other hand, if most of the heating occurs above the critical point once the flow is already supersonic and beyond the influence of its origin at the corona, the increase in energy that is provided by the heating is deposited directly to the kinetic energy of the particles in the plasma (there is no increase in mass flux or density) and the speed of the wind is increased. Thus, the fast wind is heated above and the slow wind is heated below the critical point. This assessment shows that the height of the critical point is different for various locations on the sun [12]. The high speed wind, originating from coronal holes, has a lower critical point and lower density since it receives most of its heating when it is already supersonic. The low speed wind, originating near helmet streamers, has a higher critical point and higher density since it receives most of its heating when it is still subsonic.

The fast and slow solar wind are the two varieties of the ambient or quasi-stationary solar wind. There also exist a variety of transient structures that interrupt the ambient background plasma flow. The frequency at which transient events occur on the sun depends on the stage of the solar cycle. Solar maximum conditions produce more transient events than periods of lower solar activity. Transient events in the solar wind include solar flares and coronal mass ejections. It is important to note that transient structures exist in the solar wind and they must be considered when describing the dynamics of the solar wind.

1.3 Solar Cycle

The sun reverses its polarity every eleven years during a period known as solar maximum. After approximately 22 years, the sun makes the full cycle from one polarity to the next, and then back to the original polarity. This 22 year cycle is known as the solar cycle, which consists of solar maximum and solar minimum conditions. During solar maximum, there are many active regions on the sun, which lead to a higher production of solar flares and coronal mass ejections. During solar maximum conditions, the number of sunspots visible on the surface of the sun also increases. Sunspots are cooler regions that correspond to regions of strong magnetic field lines. In between solar maximum conditions the sun settles into solar minimum. During solar minimum, there is less solar activity and therefore there are fewer sunspots and the solar wind is less variable. The sun is also highly structured during solar minimum with high speed solar wind streams emerging from the polar regions, and low speed streams originating from lower latitudes. The magnetic field of the sun is also more structured and predictable during solar minimum conditions.

The theory that describes the cause of the sun's magnetic field is known as solar dynamo theory. Although this theory describes the origin of the magnetic fields, it provides no

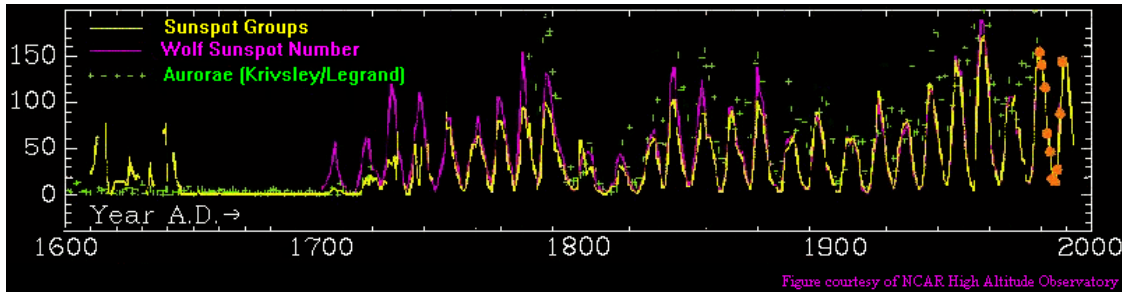


Figure 1.1: The number of observed sunspots plotted as a function of time (Image courtesy of NOAA NGDC Solar Data Services).

information as to what causes the shift in polarity every eleven years. The cause of the solar cycle is an area of active research. Sunspots have been documented through the years, and so there exists a record of solar maxima and minima. Within the database of sunspot activity, there exists a period of approximately seventy years where hardly any sunspots were observed. This epoch has been labeled the Maunder Minimum, and it spans the years 1645 to 1715 A.D. Figure 1.1 displays the sunspot number as a function of time from 1600-2000 A.D.

The number of sunspots visible on the surface of the sun isn't the only thing that changes with the solar cycle. Along with an increase in sunspots, solar maximum also brings an increase in overall magnetic field strength, and a decrease in the overall velocity of the solar wind. Solar activity is a measure of the magnetic activity of the sun. Solar maximum is a period that exhibits a lot of solar activity, and this corresponds to an increase in magnetic field activity and strength. One of the regions on the sun from which the slow wind is thought to originate is active regions. Solar maximum contains more active regions than normal, and this means that more sources of slow solar wind exist. As a result of a higher number of sources of slow solar wind during solar maximum, the overall speed of the solar wind decreases. Figure 1.2 demonstrates the effect of the solar cycle on the solar wind velocity and magnetic field. There is a strong correlation between sunspot number and magnetic field strength, and the solar wind velocity appears to be anticorrelated to the other two quantities.

1.4 Spacecraft Missions

The Helios mission consists of two spacecraft launched in a joint effort between the National Aeronautics and Space Administration (NASA) and the Federal Republic of Germany [52]. Helios 1 and 2 were launched on December 10, 1974 and January 15, 1976 respectively. The aim of the Helios mission was to make in situ observations of the solar wind in the inner heliosphere. The Helios spacecraft traveled highly elliptical heliocentric orbits that had a perihelion of 0.309 AU for Helios 1 and 0.290 AU for Helios 2. These spacecraft were the first satellites to be sent closer to the sun than the innermost planet Mercury. The orbital periods of Helios 1 and 2 were 190 and 187 days respectively. The Helios spacecraft had twelve experiments on board including plasma instruments, magnetometers, and cosmic ray instruments. The major contribution of the Helios mission is that these spacecraft provided the first in situ measurements of the interplanetary medium in the inner heliosphere, and to this day they hold the record for the closest approach to the sun.

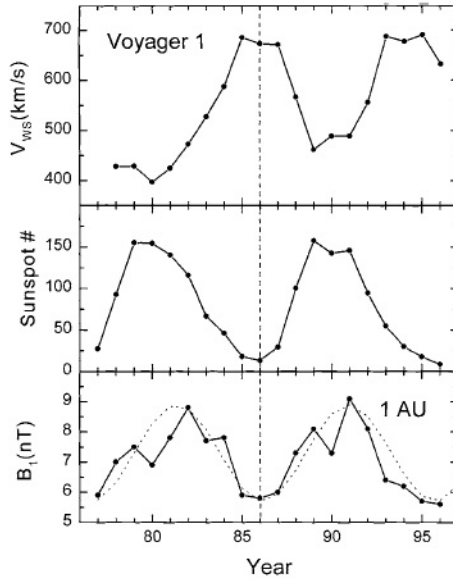


Figure 1.2: (top) Solar wind velocity as a function of time, (middle) sunspot counts over time, and (bottom) magnetic field strength at 1 AU plotted as a function of time (image courtesy of *Burlaga* [9]).

The Voyager mission consists of two identical spacecraft Voyager 1 and Voyager 2. Voyager 2 was launched on September 5, 1977 and Voyager 1 was launched August 20, 1977 [26]. The initial goal of the Voyager mission was to explore Jupiter and Saturn. The two Voyager spacecraft are still operational and in flight to this day and they have done far more than simply explore two of the giant planets. The two spacecraft did fulfill their original expectations of exploring Jupiter and Saturn and provided us with new information about the planets including discoveries of active volcanoes on Jupiter's moon Io and a better understanding of Saturn's rings [26]. The spacecraft had such success that their missions have been continuously extended and they are still traveling outwards from the sun into the outer heliosphere and approaching the local interstellar medium. In fact, it is accepted in the space science community that Voyager 1 crossed the termination shock (or was crossed by the termination shock) on December 16, 2004 at a distance of 94.0 AU from the sun [10]. Voyager 1 is traveling at an angle of approximately 34 degrees above the ecliptic plane, and Voyager 2 is traveling at an angle of about -27 degrees relative to the ecliptic. Figure 1.3 is an artist's rendition of the two Voyager spacecraft and their trajectories through the heliosphere and beyond.

The Voyager missions initially had 11 functional instruments on board to take readings of the solar wind and planetary data including optical photographs. Today, there are five investigator teams that are still supported. The Voyager missions continue to provide us with new information regarding the outer heliosphere and the termination shock. The two spacecraft are powered by the decay of Plutonium, and it is believed that the two missions will lose the power required to provide information around the year 2020. Until then, we can only hope that they will continue to function and that perhaps when Voyager 2 crosses the termination shock we will learn even more from a second crossing.

Ulysses was launched on October 6, 1990 as a joint effort between the European Space Agency (ESA) and NASA. The motivation for Ulysses was to explore the heliographic lat-

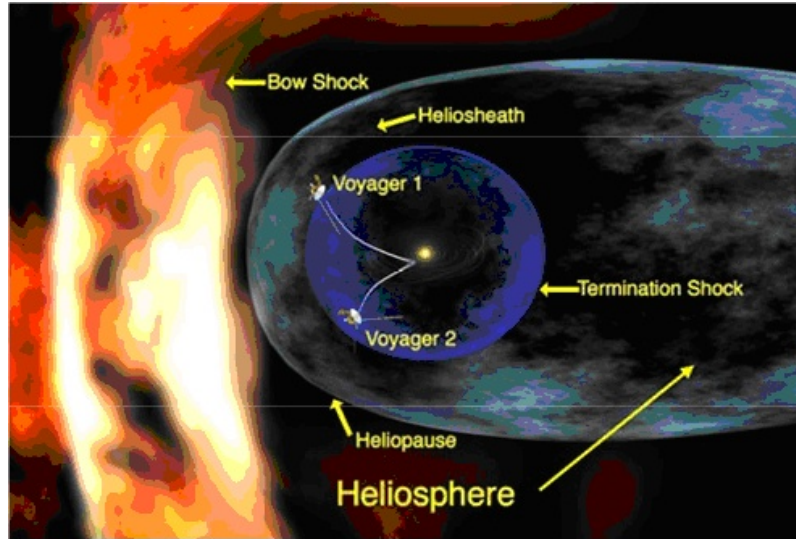


Figure 1.3: An artist’s rendition of the heliosphere and the location of Voyager 1 and 2 as they travel through the outer heliosphere and perhaps on into the interstellar medium (Image courtesy of *Feimer* [16]).

itudinal dependence of the solar wind and the structure and dynamics of the corona. In order to explore different heliographic latitudes, Ulysses must traverse a polar orbit around the sun. A polar orbit takes Ulysses out of the ecliptic plane, and such an orbit requires more energy than an orbit in the ecliptic. Scientists and engineers designed a trajectory that would make use of Jupiter’s gravitational energy in the form of a gravity assist to place Ulysses into a polar orbit. Ulysses used a gravity assist in 1992 [25], and it has been orbiting the sun in a polar orbit since that day. The intersection of Ulysses’ orbital plane with the sun’s equatorial plane is approximately 80 degrees, the perihelion of the orbit is 1.4 AU from the sun, the aphelion is 5.4 AU, and its orbital period is 6.2 years [2].

With its polar orbit, Ulysses has provided us with novel discoveries. It has confirmed the theory that the polar regions have characteristically high solar wind velocities on the order of 750 km/s, and are nearly uniform over the poles [2]. Ulysses has demonstrated a clear difference between the slow and fast solar wind temperatures and ion compositions [43]. The radial component of the sun’s magnetic field has been shown to be independent of the heliocentric latitude. Ulysses has shown that turbulence in the solar wind is slower to evolve in the polar regions than it is in the ecliptic region. It has also shown a latitudinal gradient of cosmic rays that is less than expected [25].

The Solar and Heliospheric Observatory (SOHO) was launched on December 2, 1995 with the primary goal of studying the sun “from its deep core to the outer corona, and the solar wind” [15]. SOHO was launched as a cooperative effort between ESA and NASA with a two year lifetime that has been extended several times to its current length of 11 years where it will be able to observe the sun over one complete solar cycle. SOHO orbits the L1 Lagrangian point and always faces the sun providing us with an uninterrupted view of the sun.

SOHO was launched in order to provide answers to three fundamental questions [15]. The first is an inquisition into the structure and dynamics of the interior of the sun where SOHO will use helioseismology - a practice that makes use of the elastic properties of the sun and allows for the propagation of waves. By analyzing the waves that propagate through the sun,

SOHO intends to gain a better understanding of the internal structure and dynamics of the sun. The second question SOHO hopes to answer is why does the corona exist, and how is it heated to a temperature over 150 times as hot as the photosphere? The spectrometers and imaging telescopes on SOHO will provide information that will help to answer this question. The third question SOHO was made to answer is the fundamental question I stated earlier in this thesis. That is, where does the solar wind come from, and what is the source of its acceleration?

The Advanced Composition Explorer (ACE) was launched August 25, 1997 with the primary objective of measuring the energetic particles from the sun, heliosphere, and the galaxy. ACE contains eight instruments for measuring composition, and a magnetometer to measure magnetic field strength. ACE, like SOHO, also orbits the L1 Lagrangian point where it is able to take samples of data outside the influence of the earth's atmosphere and magnetic field. There is enough fuel aboard ACE for it to remain on its L1 orbit through 2019.

Due to the fact that ACE has so many instruments on board, it is able to provide a wide range of information about solar wind properties. The mission has four main objectives [55]. The first is to provide detailed information regarding elemental and isotopic abundances of nuclei in the solar wind. ACE is able to study nuclei ranging from Hydrogen ($Z=1$) to Nickel ($Z=28$). A second task of ACE is to provide information on the origin and evolution of the elements in our solar system. It is theorized that the solar system was not homogeneous when it was formed, and also that the galaxy itself is not homogeneous. ACE will be able to provide elemental and isotopic measurements of solar material as well as that from galactic cosmic rays and from the local interstellar medium. It is able to do so because it has instruments on board capable of measuring energies ranging from solar wind energies (on the order of 1 keV/nucleon) to galactic cosmic ray energies (on the order of 500 MeV/nucleon). The third task is to study the acceleration of the solar wind and the formation of the corona. ACE will compare samples of coronal and photospheric abundances, as well as comparing features of solar energetic particles and the solar wind. The fourth major objective of ACE is to study particle acceleration and transport in nature. It is still a major objective in heliospheric studies to determine the source of heating and acceleration of the solar wind. ACE hopes to provide insight into the form of acceleration in nature by isolating "solar flare, coronal shock, and interplanetary shock acceleration models with charge, mass, and spectral data" [64].

The dynamics of a satellite interacting with the sun and earth can be represented in what is called the restricted three-body problem [17]. This problem is aimed at finding locations about the earth and sun at which there is no net force acting on the satellite. It turns out that five such locations exist. The five locations are the five Lagrangian points L1 through L5 named after Joseph-Louis Lagrange. L1 through L3 are collinear. In the sun-earth system, L1 lies between the earth and sun, L2 is on the night side of the earth, and L3 is on the opposite side of the sun from the earth. L4 and L5 lie above and below the sun-earth line. L1 through L3 are saddle points, and so they are unstable points of equilibrium. The slightest deviation from these points leads to a gravitational force that will pull the satellite towards the sun or the earth. The fourth and fifth Lagrangian points are stable regions of balanced force between the sun and earth. The satellites ACE and SOHO are both orbiting the first Lagrangian point (L1) in a halo orbit. The status of these two satellites must be checked regularly so as to keep them within the force free region of the unstable L1 point.

Chapter 2

Solar Wind Structure and Fluctuations

2.1 Parker's Model of the Solar Wind

In 1958, E. N. Parker wrote a paper that forever changed our perception of the solar wind. In his model, Parker did not deal with the issue of coronal heating. He assumed that a certain temperature level was maintained (it had been determined from absorption lines and the charge states that were deduced from these lines), and he built his model upon a corona that was sufficiently hot [45]. Parker's model sets the sun in a vacuum such that the pressure goes to zero as the radial distance from the sun goes to infinity. This model implies that the atmosphere of the sun cannot remain in static equilibrium, but that the solar atmosphere expands into space and is replaced by particles from the inner atmosphere. Therefore a continual outflow, or streaming, of particles from the sun is predicted by Parker's model. This corpuscular radiation, or stream of particles, has been labeled the solar wind.

Parker's assumptions lead to the differential equation [47]:

$$\left(\frac{V_{SW}^2}{v_s^2} - 1 \right) \frac{dV_{SW}}{V_{SW}} = \left(2 - \frac{GM}{v_s^2 r} \right) \frac{dr}{r} \quad (2.1)$$

where V_{SW} is the solar wind velocity, v_s is the velocity of sound, r is the radial distance from the center of the sun, G is the gravitational constant, and M is the mass of the sun. There are four solutions to this differential equation, but the solution that fits the conditions present in the solar wind is [47]

$$\frac{V_{SW}^2}{v_s^2} - 2 \ln \left(\frac{V_{SW}}{v_s} \right) = 4 \ln \left(\frac{r}{r_c} \right) + 4 \left(\frac{r_c}{r} \right) - 3 \quad (2.2)$$

where $r_c = \frac{GMm}{4kT}$ is the 'critical point' where the solar wind becomes supersonic. Parker [46] explains the transition from subsonic to supersonic flow in the solar wind with an analogy to a Laval nozzle. A Laval nozzle is a tube that has a pinch in the middle to form an hour glass shape. Gas flows through the nozzle and is accelerated from subsonic to supersonic speeds as it passes through the throat of the nozzle. Parker relates the throat of the nozzle to the force of gravity acting on the solar wind. In the instance of the solar wind, the velocity is subsonic until it reaches the critical point and the flow becomes supersonic.

Figure 2.1 provides a graph of theoretical predictions from Parker's model of the solar wind velocity as a function of radial distance from the sun for various coronal temperatures.

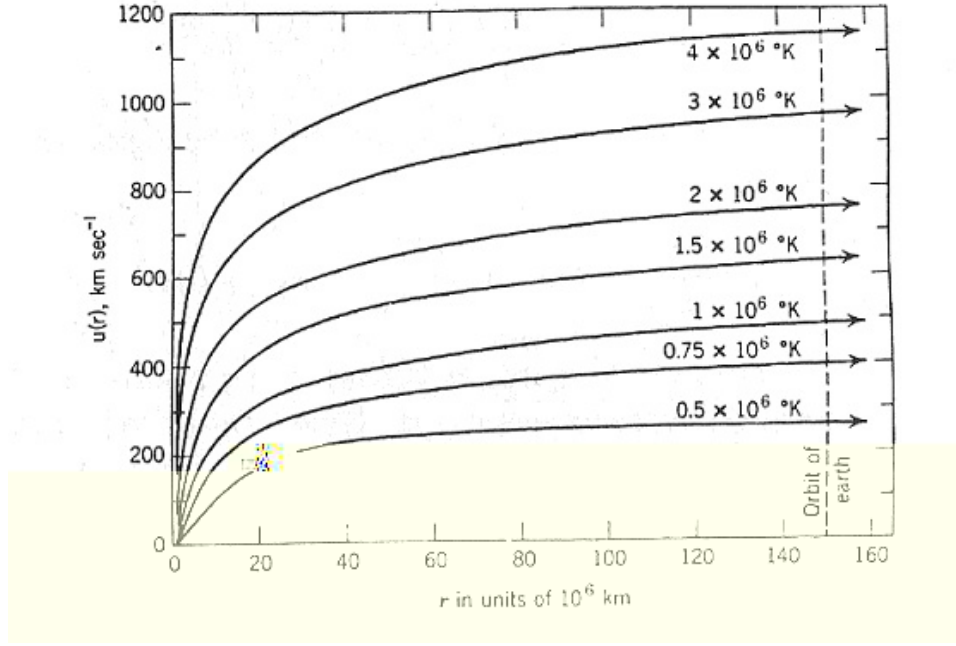


Figure 2.1: Solar wind velocity plotted against the radial distance from the sun as predicted by Parker’s solar wind model described by equation 2.2 (Image courtesy of *Kallenrode* [?]).

At the earth’s orbital distance from the sun, the predicted solar wind velocity ranges from around 200 km/s to 1100 km/s corresponding to coronal temperatures of $(5 - 40) \times 10^5$ K.

In situ observations of the solar wind taken by the Soviet spacecraft Lunik 2 and 3 were sporadic and inconsistent [23], but the American spacecraft Mariner 2 provided consistent readings and a confirmation that the solar wind flows at supersonic speeds as predicted by Parker’s model of the solar wind. The term ‘supersonic’ isn’t technically correct. When using the term ‘supersonic’, I really mean super-Alfvénic. Alfvén waves (see Section 2.3) are the waves that propagate in interplanetary space, and the solar wind becomes ‘supersonic’ when the wind travels at a rate faster than the waves within it propagate (the Alfvén speed). Therefore, when I use the term ‘supersonic’ I am actually referring to super-Alfvénic. The results of Advanced Composition Explorer observations are shown in Figure 2.2. The solar wind V_P is measured to flow between 400 km/s to 800 km/s, which is well within the predictions made by Parker’s solar wind model. These observations show a general anticorrelation between the solar wind velocity and density. This topic of the density and the velocity of the solar wind was described in Section 1.2.

In his 1958 paper Parker also provided a theoretical prediction of the interplanetary magnetic field. Parker’s magnetic field model is based upon the following assumptions [9]: The solar wind flows radially outward from the sun at a constant velocity V_{SW} . The sun rotates at an angular speed Ω that is found by dividing 2π by the solar rotation period of approximately 27 days. The solar wind is azimuthally symmetric about the rotation axis of the sun, and the interplanetary magnetic field is frozen into the solar wind and has its feet anchored at the sun.

The Parker prediction for the magnetic field in the equatorial plane of the sun is an Archimedes spiral. Figure 2.3 is taken from Parker’s 1958 paper and demonstrates the orientation of the interplanetary magnetic field in the ecliptic plane. This figure extends

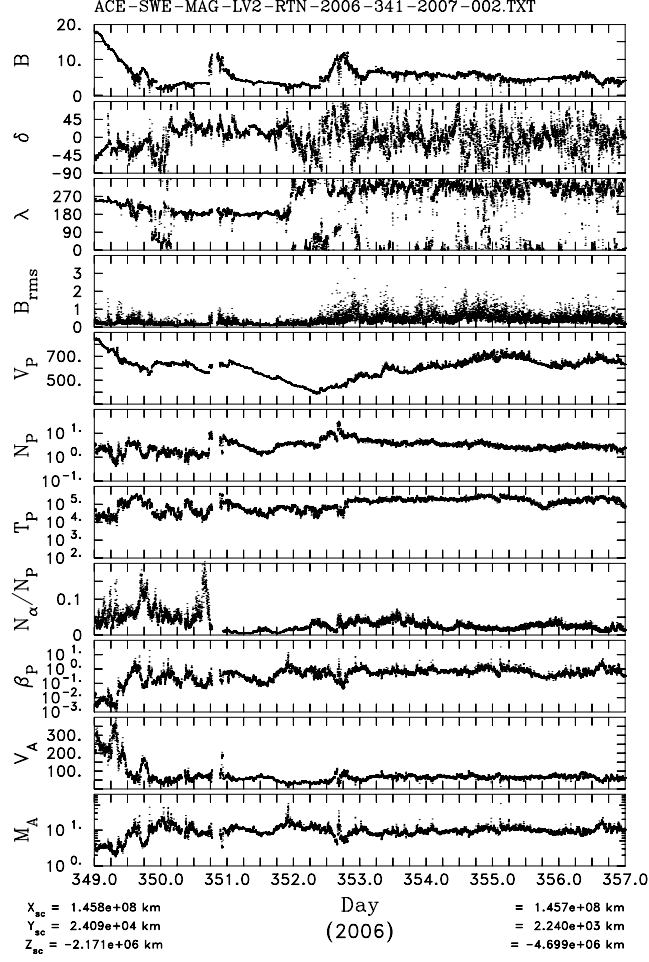


Figure 2.2: Advanced Composition Explorer solar wind observations for one week. The fifth panel from the top displays the solar wind velocity in units of km/s. (Image courtesy of the ACE MAG team).

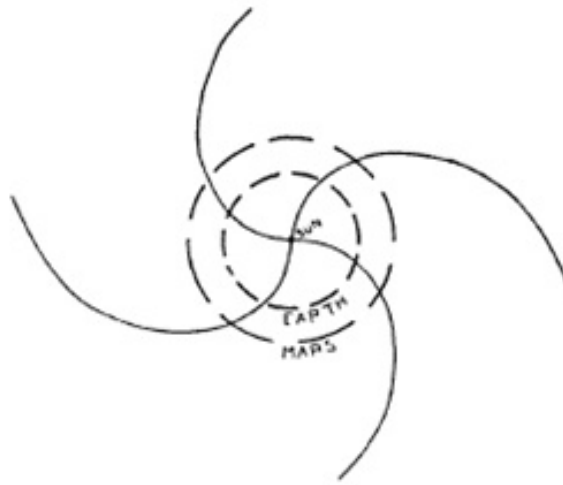


Figure 2.3: The Archimedes spiral of the orientation of the interplanetary magnetic field predicted by Parker’s model of the solar wind (Image courtesy of *Parker* [45]).

the field to just beyond the orbit of Mars, but the theory predicts an extension of this field into the outer heliosphere until this structured nature is disrupted at the termination shock where the solar wind is slowed to subsonic speeds as it meets the interstellar medium.

In his model of the interplanetary magnetic field, Parker described the strength of the large scale magnetic field as the square root of the sum of the squares of each component. Parker’s equation for the strength of the magnetic field is a function of source strength, heliographic latitude, radial distance from the sun, and solar wind velocity.

Many spacecraft have carried magnetometers and in Section 1.4 I described that the two Voyager spacecraft are traveling through the outer heliosphere. Figure 2.4 shows the theoretical predictions of Parker’s magnetic field strength plotted on the same grid as the observed magnetic field strength measured by Voyager 1. It is apparent from the plot that Parker’s theoretical prediction is in very close agreement with empirical observations.

2.2 Interplanetary Magnetic Field

Solar dynamo theory explains the creation of the solar magnetic field. I will not discuss solar dynamo theory in this paper, but I will discuss the sun’s magnetic field and its presence in the solar wind. The solar cycle (see Section 1.3) affects the strength and polarity of the sun’s magnetic field. The polarity reverses every eleven years, and after each eleven year half-cycle, during solar maximum, is when the polarity reverses. During solar maximum conditions, the polarity of the field isn’t well-behaved or structured at all. In between transition stages, during solar minimum, the magnetic field of the sun is highly structured. The Parker spiral that was first proposed by Parker in his 1958 paper is still used today to describe the orientation of the interplanetary magnetic field. The continual stream of plasma from the solar source, combined with the approximate 27 day rotation period of the sun produce an Archimedes spiral that originates at the sun and extends out into the interplanetary medium.

At the location of earth, one astronomical unit from the sun, the magnetic field is usually

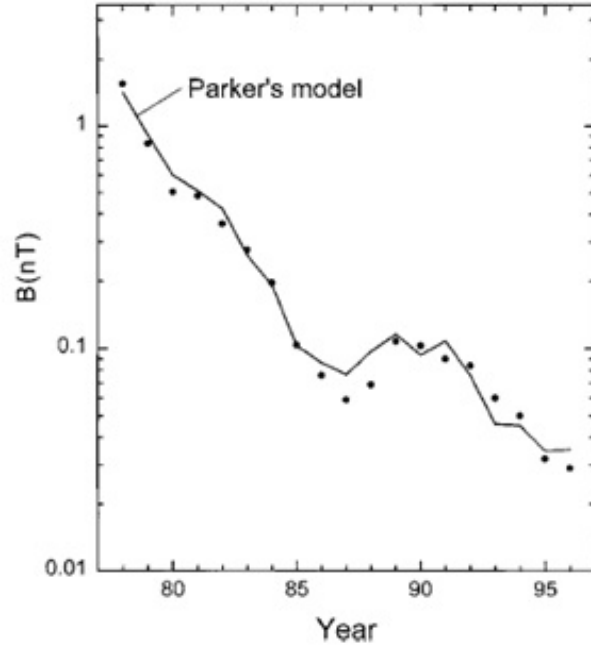


Figure 2.4: Magnetic field strength as a function of time predicted by Parker (solid line) and observed by Voyager 1 (circles) (Image courtesy of *Burlaga* [9]).

oriented at a 45 degree angle from the radial direction. At the beginning of solar minimum conditions, in situ observations taken at earth normally show inward- (outward-) oriented magnetic field for the first half of the solar rotation, and outward- (inward-) oriented magnetic field for the second half of the solar rotation. A solar rotation as seen by an observer at earth has duration of approximately 27 days, and so each orientation will span about 14 days. These time periods of uniform magnetic field orientation are known as sectors [9]. The start of solar minimum therefore contains a two sector structure. During the middle of solar minimum, observations have shown that a four sector structure exists [9], and solar maximum, since it is so variable and unpredictable, usually contains no such magnetic field structure. The four sector structure has alternating intervals of field orientation, and each sector has equal duration of approximately 7 days each.

The magnetic sector pattern that is observed in the solar wind is an extension of the sun's magnetic field into the solar wind. The two sector pattern corresponds to a magnetic dipole structure at the sun, the four sector pattern is a result of a quadrupole structure, and the lack of a sector pattern during solar maximum reflects the lack of a structure in the sun's magnetic field at this time. The extension of the heliomagnetic equator into the heliosphere is known as the heliospheric current sheet [9], and it is a plane of neutral magnetic orientation. Figure 2.5 is a model of what the heliospheric current sheet might look like. This current sheet is not a perfectly level plane, but it varies its shape as a function of the solar cycle. When the two sector structure is observed and the sun behaves as a magnetic dipole the heliospheric current sheet is a fairly level surface, but the four sector pattern and the magnetic quadrupole behavior of the sun distorts the current sheet, and during solar maximum conditions the structure and orientation of the current sheet is highly variable and unpredictable.

When describing the solar wind, it is important to discuss some of the global properties it

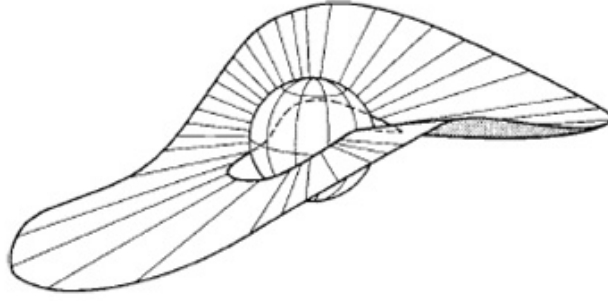


Figure 2.5: A model of the heliospheric current sheet (Image courtesy of *Burlaga* [9]).

Table 2.1: Global Properties of the Solar Wind (Data courtesy of *Schwenn* [56])

Parameter	Common Physical Parameters	
	Solar Wind Values	Terrestrial Values
Flow Speed (km/s)	average ~ 350	Speed of Sound ~ 0.34
Density (particles/cm ³)	~ 9	At Sea Level $\sim 10^{18}$
Temperature (K)	protons $\sim 4 \times 10^4$	Room $\sim 3 \times 10^2$
	electrons $\sim 1.5 \times 10^5$	no free electrons
Magnetic Field (Tesla)	5×10^{-9}	$(3 - 6) \times 10^{-5}$

exhibits. The solar wind is a current-conducting, magnetic field-carrying, supersonic-flowing plasma. Table 2.1 gives a summary of some of the key features shown by the solar wind and puts these values into perspective by comparing them to some more familiar terrestrial values.

2.3 Plasma Waves in the Solar Wind

The solar wind is a plasma, and so the waves that propagate through the solar wind are plasma waves. Since the density of the solar wind is so low (~ 9 protons/cm³) the mean free path - the mean distance a particle travels before colliding with another particle - is approximately one astronomical unit [48]. Instead of the normal physical collisions between particles that is seen in a hydrodynamic gas, particles within a magnetohydrodynamic (MHD) fluid such as plasma normally interact via plasma waves. Plasma waves carry energy and momentum in the solar wind and are believed to be responsible for much of the heating and acceleration of the solar wind [21].

Multiple types of plasma waves exist, and the propagation velocity of these waves is dependent upon several factors including [21] the speed of light (c), magnetic field strength (B), particle number density (N_s), and the particle temperature (T_s). The subscript ‘s’ refers to the species of the plasma wave where $s = e$ corresponds to electrons and $s = i$ corresponds to ions. Plasma waves are usually described as a function of frequency, and some common frequencies include [21] the electron cyclotron frequency ($f_{ce} = (1/2\pi)eB/m_e$, where e is the elementary charge and m_e is the mass of the electron), the ion cyclotron frequency ($f_{ci} = (m_e/m_i)f_{ce}$, where m_i is the mass of the ion), the electron plasma frequency ($f_{pe} = (1/2\pi)(N_e e^2/\epsilon_0 m_e)^{1/2}$, where ϵ_0 is the permittivity of free space), and the ion plasma

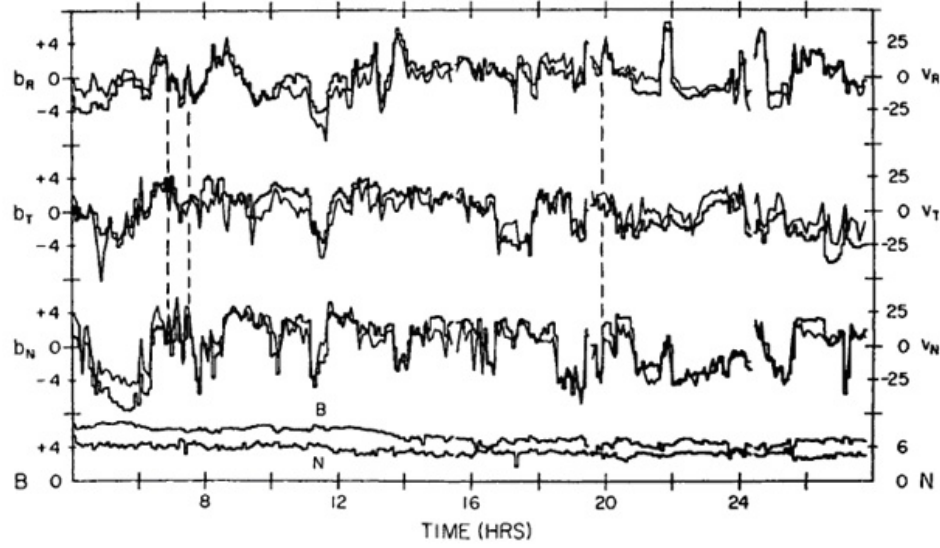


Figure 2.6: Observations of the magnetic field strength and velocity in three components, and the magnitude of the magnetic field and density provided by Mariner 5 (Image courtesy of *Belcher and Davis* [5]).

frequency ($f_{pi} = (m_e/m_i)^{1/2} f_{pe}$).

The most important reference velocity in plasmas is the Alfvén speed [21] ($V_A = B/(\mu_0 \rho_m)^{1/2}$, where μ_0 is the permeability of free space and ρ_m is the mass density). The Alfvén speed is the speed at which Alfvén waves propagate through a plasma. An Alfvén wave is a transverse wave that is the fluctuation of the magnetic field. If one pictures the magnetic field as a taut string, the Alfvén wave is analogous to the transverse wave that travels along the string if the string is plucked. The solar wind has both massive particles in the form of a plasma and a magnetic field in the form of the IMF. When the magnetic field is disturbed, waves are created in the plasma by the restoring force of the magnetic field. Such waves are known as Alfvén waves. Other important speeds in the solar wind are the electron sound speed ($V_e = \gamma k T_e / m_e)^{1/2}$, where γ is the adiabatic compression factor, and k is the Boltzmann constant), and the ion sound speed ($V_s = \gamma k T_i / m_i)^{1/2}$) [21].

Three of the plasma waves are MHD waves; the fast mode, slow mode, and Alfvén waves. The sound speed V_s corresponds to the electron sound speed for electron waves, and to the ion sound speed for ion waves. Alfvén waves were discovered by *Alfvén* [1] and were shown to exist in the solar wind by *Unti and Neugebauer* [66] and *Belcher et al.* [4]. The fast mode wave has higher characteristic velocities than Alfvén mode wave which in turn has a higher characteristic velocity than the slow mode wave.

Figure 2.6 provides evidence for the existence of Alfvén waves in the solar wind. The plot contains velocity and magnetic field observations superimposed on the same plot, and the values along each direction b_r , b_t , and b_n are stacked on top of one another. The bottom plot contains the magnitude of the magnetic field and the density of the solar wind. The magnetic field and velocity are measured in the RTN coordinate system. This coordinate system has its origin at the sun and the R component is the radial direction from the sun to the spacecraft making measurements. If ω is the unit vector that points in the direction of the sun’s spin axis, the T component of the RTN coordinate system is in the direction of the vector resulting from $\omega \times R$, and N is the unit vector in the direction of $R \times T$ to complete the right-handed

coordinate system. The fluctuations of magnetic field strength and propagation velocity in each component shown in Figure 2.6 are Alfvén waves. It is clear that these fluctuations are Alfvén waves because there exists a variation of each individual spatial component of the solar wind, but no variation in the overall magnitude or density of the solar wind. Alfvén waves are transverse waves, not compressive waves, and the characteristics demonstrated in Figure 15 indicate that the observed fluctuations are Alfvén waves.

2.4 Wave Vectors in the Solar Wind

As stated in Section 2.3, Unti and Neugebauer [66] and Belcher et al. [4] demonstrated the existence of Alfvén waves in the solar wind. Two years after their initial paper on the subject, Belcher and Davis showed fluctuations in velocity and the magnetic field to be primarily transverse to the mean magnetic field. It is worth noting that these studies made use of low frequency observations. This work is often interpreted in terms of the minimum variance direction. In the case of fluctuations transverse to the magnetic field, the minimum variance direction is along the field. In the early studies of waves in the solar wind, it was assumed that the minimum variance direction was the same as the wave vector orientation. A predominant model used at the time for describing fluctuations of the interplanetary magnetic field is that all fluctuations arise from non-interacting, outward propagating Alfvén waves that move in the direction parallel to the mean magnetic field. With this description and the assumption that the minimum variance direction is equivalent to the wave vector orientation, all wave vectors and minimum variance directions would be along the mean magnetic field. However, wave vectors may be oriented both perpendicular and parallel to the mean field while the minimum variance direction is parallel to the mean field. The minimum variance direction should not be equated with wave vector orientations.

The issue of wave vector orientation was addressed by *Matthaeus et al.* [39] using a correlation function of the magnetic field. The result of the analysis has come to be known as the Maltese cross. This Maltese cross demonstrates that there is a strong wave vector orientation in both the one-dimensional field-aligned component and the two-dimensional plane perpendicular to the mean magnetic field, but not much in between. Although the assumption that the wave vectors are a composite of strictly parallel and strictly perpendicular orientations is a simplification of the true situation in the solar wind, it is a useful model that permits the extraction of the amount of energy contained in the two components. Building upon the results of the Maltese cross, *Dasso et al.* [13] compute magnetic and velocity correlation functions using solar wind observations provided by the ACE spacecraft, but they perform the analysis on the basis of wind speed. Defining the fast solar wind to be intervals with an average wind speed greater than 500 km/s and the slow solar wind to be intervals with an average wind speed less than 400 km/s, they find the fast wind to be largely populated by wave vectors aligned with the magnetic field and the slow wind to be populated by wave vectors perpendicular to the magnetic field.

Motivated by the implications of the Maltese cross, *Bieber et al.* [6] derive a method for determining the relative amount of energy contained in the wave vectors parallel and perpendicular to the magnetic field (see Section 5.5 for an analytical description of the Bieber method). This derivation relies upon the simplification that wave vectors in the solar wind are oriented either perfectly parallel or perpendicular to the mean magnetic field. Again we note that this case is an over-simplification but allows a distinction to be made between the two components that are clearly demonstrated to exist by *Matthaeus et al.* [39]. *Bieber*

et al. apply the test for determining the amount of energy in the parallel and perpendicular components to observations of the solar wind made by the Helios spacecraft. They find that 80% of the energy is contained in the two dimensional component perpendicular to the mean magnetic field. These results are in stark contrast with the assumption that fluctuations of the solar wind are caused primarily by non-interacting Alfvén waves with wave vectors aligned with the magnetic field. It is evident that there are other causes for solar wind fluctuations. The non-linear interactions associated with magnetohydrodynamic turbulence is one such possible cause.

2.5 Heating of the Solar Wind

Observations from the Helios spacecraft taken inside 1 AU demonstrate isotropic velocity distribution functions for thermal ions [33]. The proton temperature in the fast wind is higher for wave vectors perpendicular to the magnetic field than for vectors aligned with the mean field ($T_{\perp} > T_{\parallel}$). The opposite is true in the slow wind. Cyclotron resonance increases the temperature of wave vectors perpendicular to the magnetic field. Landau resonance is a phenomenon that affects charged particles in the solar wind traveling in the longitudinal direction. Therefore, the temperature of wave vectors parallel to the mean field is increased by Landau resonance.

Although the temperature profile in wave vectors perpendicular and parallel to the magnetic field in the solar wind is an interesting topic, what is more relevant to this paper is the radial variation of the temperature with increasing distance from the sun. If the solar wind were to expand adiabatically, the temperature as a function of distance r from the sun would be proportional to $r^{-4/3}$. In situ measurements of the solar wind taken by Helios [18], and Voyager [53] have shown that the temperature of the solar wind decreases slower than an adiabatic expansion would predict. By 15 AU the solar wind is $10\times$ hotter, and by 70 AU the solar wind is $100\times$ hotter than the adiabatic prediction. The departure from an adiabatic cooling process indicates the presence of a source of heating in the solar wind.

Zhou and Matthaeus [71], *Zank et al.* [70], and *Matthaeus et al.* [41] have shown that a turbulent transport model based on the large energy-containing scales of magnetohydrodynamic (MHD) turbulence can provide the right amount of energy cascade to resupply the dissipation process in a continuous fashion and thereby account for the heating of the solar wind. Their model does not assume any particular dissipation process, but assumes that the inertial range is energy-conserving so that the energy cascade rate in the inertial range will be equal to the heating rate in the dissipation range. This model does assume the fluctuations are two-dimensional and that the cascade of energy to the dissipation range is two-dimensional in nature. Section 2.4 demonstrates the existence, and in some cases the dominance, of 2D fluctuations in the solar wind which validates the assumption of a 2D cascade. *Smith et al.* [59, 60] demonstrate that a turbulent transport model, together with the *Isenberg et al.* [24] analysis of the pickup ion process, can account for thermal proton energies to 75 AU where their analysis stops for reasons of data availability.

Chapter 3

Solar Wind Turbulence

3.1 Interplanetary Spectrum

The model of solar wind turbulence I employ is based on the power spectrum of fluctuations depicted in Figure 3.1. The turbulent energy is generated at the low frequencies and large length scales of the energy containing range. The energy is then fed through the energy conserving intermediate scales of the inertial range. The turbulent energy is then converted to heat energy at the small scales of the dissipation range.

3.2 Energy-Containing Range

The energy-containing range is characterized by a f^{-1} form when looking at power spectra of the interplanetary magnetic field. The $q = -1$ power law index is typically found at frequencies below $1/T_c$ where $T_c \sim 3.4$ hours is the average correlation time of the interplanetary magnetic field [36]. *Matthaeus and Goldstein* [37] study the f^{-1} noise in the interplanetary magnetic field. They explain that the source of the interplanetary fluctuations at these low frequencies is a product of magnetic structures on the surface of the sun. The fact that the energy containing range occurs at frequencies lower than $1/T_c$ means that fluctuations on this time scale (which are greater than the correlation time) are uncorrelated events that have their source at the sun. There have been turbulent transport models proposed to account for the nonadiabatic expansion of the solar wind [71, 70, 41]. These models rely on the presence of energy in the large scales of the energy-containing range to drive turbulence in the smaller scales where the energy is ultimately dissipated to heat the background plasma. As stated in Section 2.5, *Smith et al.* [59, 60] and *Isenberg et al.* [24] demonstrate that these models of turbulent transport and the added heating provided by pickup ions in the outer heliosphere account for the amount of energy required to produce the heating of the solar wind that is observed. Thus the connection between the energy contained in the large scale fluctuations in the solar wind and the heating of the background plasma is successfully made.

3.3 Inertial Range

In between the large scale fluctuations in which the energy is contained and the small scale fluctuations at which the fluid energy is dissipated as heat lies the inertial range. The inertial range is a self-similar, energy conserving pipeline through which energy travels before it is

Model of Solar Wind Turbulence

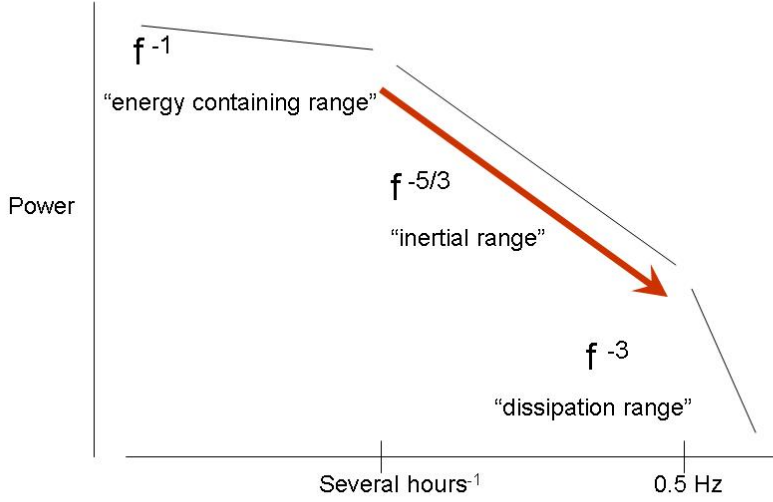


Figure 3.1: A model power spectrum of interplanetary turbulence displaying the energy containing, inertial, and dissipation ranges.

dissipated as heat energy in the dissipation range. In this range of frequencies, power spectra of the fluctuations of the interplanetary magnetic field are characterized by a power law index $q = -5/3$. A.N. Kolmogorov made significant contributions to our understanding of inertial range properties in hydrodynamic turbulent flows. In a theory that predicted the energy cascade rate in the solar wind, Kolmogorov proposed a $-5/3$ power law index in the inertial range of homogeneous turbulence. One reason that we have been able to successfully adapt the hydrodynamic model of turbulence for solar wind studies is because this same $f^{-5/3}$ form is observed in magnetic field fluctuations. However, *Podesta et al.* [49] demonstrate a $f^{-3/2}$ form in the power spectra of velocity fluctuations. This $q = -3/2$ spectral index is in agreement with the predictions of *Kraichnan* [30]. Kraichnan postulates a $f^{-3/2}$ form of the power spectra for both velocity and magnetic field fluctuations in a MHD fluid. *Leamon et al.* [31], *Podesta et al.* [49], and *Hamilton et al.* [22] demonstrate that the power spectra of magnetic fluctuations in the solar wind exhibit a $f^{-5/3}$ spectral form. Some of the work presented in this thesis is done with an assumed Kolmogorov power law behavior with the power law index $q = -5/3$. This assumption is well supported by observations of the power law index in the inertial range, which are closer in agreement with the Kolmogorov $q = -5/3$ than the Kraichnan $q = -3/2$ (see Table 4.1 and Figure 5.8).

In the same year that Kolmogorov described the rate of energy cascade ϵ through the inertial range as a function of the power spectrum of velocity fluctuations, he also derived a more fundamental method of determining the cascade rate based on the third-order structure function. The first relation was primarily a result of unit analysis whereas the structure function method is derivable from the non-linear terms of the Navier-Stokes equations. For a more detailed discussion of the two methods see Section 4.2. The final two chapters of this thesis analyze two aspects of solar wind turbulence in the inertial range. Chapter 4 studies

the cascade of energy in the solar wind at 1 AU using measurements of the low-frequency end of the inertial range. Chapter 5 studies turbulent properties at various locations in the inner heliosphere at higher frequencies to determine whether there is a spatial evolution of the turbulence as the solar wind expands from 0.3 to 1 AU.

3.4 Dissipation Range

The physical processes taking place within the small scales of the dissipation range are not well known, but spacecraft have made in situ observations of this region to understand some of its turbulent properties. The onset of the dissipation range is usually found at several tenths of a Hz [31, 62] and typically has an average f^{-3} power law form in the magnetic field [31, 22]. This $q = -3$ index is an average value, and power spectra are known to have both steeper and shallower power law indices. In fact, *Leamon et al.* [31] demonstrate that the spectral index of the dissipation range is dependent on the temperature of the background plasma; the intervals with higher temperatures have steeper power law indices indicating a higher rate of energy dissipation. *Smith et al.* [62] measure both the energy cascade rate in the inertial range and the power spectral index in the dissipation range and find the two quantities to be directly related. They show that higher energy cascade rates in the inertial range lead to steeper power law indices in the dissipation range. At the length scales of the dissipation range, the energy that travels through the inertial range from the energy-containing range is dissipated to heat the background plasma. Although the fluid approximation used to describe the turbulence in the solar wind is very successful in describing many observed properties, at the small scales involved with the dissipation range there is a breakdown of the single fluid model. It is likely that in the dissipation range there exists a transition from fluid turbulence to the dominance of kinetic physics in the solar wind.

3.5 Published Papers

Up to this point my thesis has been a description and explanation of various properties of the solar wind that can be understood on the basis of previous research that has been done in the field. The following two chapters are the result of original research that I have been a part of during my time here at the University of New Hampshire. Chapter 4 is a modified version of the journal article “The Turbulent Cascade at 1 AU: Energy Transfer and the Third-Order Scaling for MHD” by B.M. MacBride, C.W. Smith, and M.A. Forman, which is being submitted to *The Astrophysical Journal*. I am the primary author of this paper and the paper has had writing and theoretical input from coauthors C.W. Smith and M.A. Forman. Chapter 5 is the first draft written only by myself of a journal article “Inertial-Range Anisotropies in the Solar Wind from 0.3 to 1 AU: Helios Observations” by B.M. MacBride, C.W. Smith, and B.J. Vasquez, which will be submitted to the *Journal of Geophysical Research* this summer.

Chapter 4

Third Moment of Fluctuations in the Solar Wind

4.1 Introduction

In Section 2.5 we discuss the need for a source of heating in the solar wind as a result of a departure from an adiabatic expansion. We also refer to a turbulent transport model that provides the proper amount of energy to account for the heating of the solar wind. Using the model of Chapter 3 where turbulent energy is generated at the large scales of the inertial range, fed through the intermediate scales of the inertial range, and converted to heat energy at the small scales of the dissipation range, we seek to determine the cascade rate for energy within the inertial range of interplanetary fluctuations. The energy driven by the large-scale structures in the energy containing range must pass through the inertial range. It is difficult to measure the energy content of the largest scales. Moreover, confirmation of the turbulent transport theories requires that the energy be tracked through the intermediate scales if we are to believe that a spectral cascade in the manner analogous to hydrodynamic turbulence exists and is responsible for the heating of the solar wind.

In the sections that follow we outline a multidimensional extension of structure function expressions derived to permit direct measurement of the energy cascade at inertial range scales. We go on to apply these expressions to Advanced Composition Explorer (ACE) measurements at 1 AU. We find that it is possible to determine the energy cascade rate and that it matches the expected value required to explain in situ heating at 1 AU. We also find that fast winds demonstrate slightly higher heating rates than slow winds. In the case of slow wind intervals we find clear evidence that the wind is evolving toward an equipartition between inward and outward propagating fluctuations by a stronger damping of the dominant outward propagating component. However, we find evidence that the fast wind is evolving to enhance the dominance of the outward propagating component by a stronger damping of the inward propagating component. This suggests that high-speed winds at greater heliocentric distances should continue to exhibit a high degree of cross-correlation between magnetic and velocity fluctuations.

4.2 Theory

Kolmogorov's landmark conclusions of 1941 provided two independent and complementary expressions describing the cascade of energy through the turbulent hydrodynamic (HD) spectrum. *Kolmogorov* [28] predicted that the omnidirectional inertial range spectrum for fully developed, stationary, and isotropic hydrodynamic turbulence would follow a power law form:

$$P(k) = C_K \epsilon^{2/3} k^{-5/3} \quad (4.1)$$

where $P(k)$ is the power integrated over wave numbers with magnitude from $|k|$ to $|k + dk|$, $C_K \simeq 1.6$ is the so-called ‘‘Kolmogorov constant’’, and ϵ is the rate of energy cascade through the spectrum. Although the above expression was derived to explain HD turbulence, it seems reasonable to apply it to MHD turbulence in case it should yield good comparisons with the inferred heating rate. *Leamon et al.* [32] demonstrate this using the measured spectrum of magnetic fluctuations and correcting for the difference between the omnidirectional spectrum referred to in eq. 4.1 and the reduced spectra that are measured with single spacecraft in the solar wind. We can rewrite the Leamon et al. result to use wavenumber spectra

$$\epsilon_P = \left[\frac{5}{3} P(|k_r|) C_K^{-1} \right]^{3/2} |k_r|^{5/2}. \quad (4.2)$$

We add the subscript ‘‘ P ’’ above since the expression yields an estimate for ϵ based on the power spectrum alone.

One added complication of MHD over HD turbulence is the existence of the Elsässer variables [14]:

$$Z^\pm \equiv V \pm B / \sqrt{4\pi\rho} \quad (4.3)$$

and the fact that these variables introduce a symmetry to the MHD equations. Noting that energy levels of Z^\pm can differ, *Matthaeus and Zhou* [38], *Zhou and Matthaeus* [71] and *Marsch* [34] derive a generalized Kolmogorov phenomenology that takes into account the power spectra of Z^\pm to write ([68], eq. 7)

$$\epsilon_P^\pm = C_K^{-3/2} P^\pm(|k_r|) \left[P^\mp(|k_r|) \right]^{1/2} k_r^{5/2} \quad (4.4)$$

where P^\pm are the intensities of the power spectra for Z^+ and Z^- , respectively, and the total energy cascade rate is $\epsilon_P^T = (\epsilon_P^+ + \epsilon_P^-)/2$. This introduces a basic asymmetry for solar wind turbulence studies since it is long recognized that outward propagating fluctuations dominate energetically over inward propagating fluctuations at 1 AU [66, 4]. The relation between Z^\pm and $Z^{in/out}$ is such that when the interplanetary magnetic field is oriented radially away from the sun ($B_R > 0$) $Z^\pm = Z^{in/out}$ and when the magnetic field is oriented radially toward the sun ($B_R < 0$) $Z^\pm = Z^{out/in}$. where B_R is the radial component of the interplanetary magnetic field (IMF). Using this relation we can write

$$\epsilon_P^{in/out} = C_K^{-3/2} P^{in/out}(|k_r|) \left[P^{out/in}(|k_r|) \right]^{1/2} k_r^{5/2} \quad (4.5)$$

if the spectral index of the power spectrum is in good agreement with the $-5/3$ prediction of *Kolmogorov* [28]. As with the above relation we can write $\epsilon_P^T = (\epsilon_P^{in} + \epsilon_P^{out})/2$.

4.2.1 Structure Function Formalism

In the same year, Kolmogorov derived a more general and analytically superior expression based on the third-order structure function that does not require a $k^{-5/3}$ inertial range spectrum and which is applicable throughout the inertial range [29]:

$$\begin{aligned} S_3^{HD}(\mathbf{L}) &\equiv \left\langle [V_{\parallel}(\mathbf{x} + \mathbf{L}) - V_{\parallel}(\mathbf{x})]^3 \right\rangle \\ &= -(4/5)\epsilon^{HD}|\mathbf{L}| \end{aligned} \quad (4.6)$$

where \mathbf{L} is the separation vector, V_{\parallel} is the component of the velocity fluctuation parallel to the separation vector $V_{\parallel} \equiv \mathbf{V} \cdot \mathbf{L}/L$ where $L = |\mathbf{L}|$, $\langle \dots \rangle$ denotes ensemble average, and ϵ^{HD} is the rate of energy cascade defined for the hydrodynamic system.

Politano and Pouquet [50, 51] have extended the *Kolmogorov* concept to address the turbulent cascade within a magnetohydrodynamic (MHD) system based on the Elsässer variables. Their expression for isotropic geometry can be applied to the supersonic flow of the solar wind according to:

$$\begin{aligned} {}^{ISO}D_3^{\pm}(L) &\equiv \left\langle \Delta Z_R^{\mp}(L) \sum_i [\Delta Z_i^{\pm}(L)]^2 \right\rangle \\ &= -(4/D)\epsilon^{\pm}L \end{aligned} \quad (4.7)$$

where $\Delta Z(L) \equiv Z(x+L) - Z(x)$ is the difference between Z measured at two points separated by a distance L , the equations for ϵ^+ and ϵ^- correspond to the cascade rate for the Z^+ and Z^- components, D is the dimensionality (assumed = 3 for spherically isotropic turbulence), and subscript “ R ” denotes the Radial component. When the energy cascade is positive and energy moves from large to small scales, cascade rates are synonymous with dissipation rates. All lagged separations are along the solar wind flow direction, \hat{e}_R , and the sign conforms to the convention that positive distances correspond to negative time lags in the data set:

$$\begin{aligned} {}^{ISO}D_3^{\pm}(\tau) &\equiv \left\langle \Delta Z_R^{\mp}(\tau) \sum_i [\Delta Z_i^{\pm}(\tau)]^2 \right\rangle \\ &= (4/3)\epsilon^{\pm}V\tau \end{aligned} \quad (4.8)$$

The total energy dissipation rate per unit mass, ϵ , is given by

$$\epsilon^T = (\epsilon^+ + \epsilon^-)/2. \quad (4.9)$$

Matthaeus et al. [39] demonstrate that the IMF fluctuations at 1 AU and at larger spatial scales than those studied here are a composite of field-aligned and perpendicular wave vectors. *Dasso et al.* [13] used this same ACE data set to show that the field-aligned and perpendicular wave vectors are spatially separated with field-aligned wave vectors in the fast wind and perpendicular wave vectors in the slow wind. Both Matthaeus et al. and Dasso et al. show power confined to parallel and perpendicular directions, preferentially. Therefore, we would like to have a formulation of the above theory that can address specifically the field-aligned and perpendicular wave vectors. We do this by first rotating the data into the mean field coordinates *Belcher and Davis* [5] and *Bieber et al.* [6] where:

$$\hat{e}_x \equiv (\hat{e}_R \times \hat{e}_B)/|\hat{e}_R \times \hat{e}_B|, \quad (4.10)$$

$$\hat{e}_y \equiv \hat{e}_z \times \hat{e}_x, \quad (4.11)$$

$$\hat{e}_z \equiv \hat{e}_B. \quad (4.12)$$

If we adopt the $2\frac{1}{2}$ D MHD geometry where the magnetic and velocity fluctuations are allowed to have all three components but the wave vectors are confined to the 2D plane perpendicular to the mean magnetic field, we may follow the *Politano and Pouquet* formalism for this reduced set of wave vectors and write:

$$\begin{aligned} {}^{2D}D_3^\pm(\tau) &\equiv \left\langle \Delta Z_y^\mp(\tau) \sum_i [\Delta Z_i^\pm(\tau)]^2 \right\rangle \\ &= 2\epsilon^\pm V \tau \sin(\Theta_{BR}) \end{aligned} \quad (4.13)$$

where V is the average solar wind speed, Z_y is the Elsässer fluctuation measured along the direction \hat{e}_y , and Θ_{BR} is the angle between the mean field direction and the flow velocity.

For MHD geometries where the wave vector is along the mean field we may similarly write:

$$\begin{aligned} {}^{1D}D_3^\pm(\tau) &\equiv \left\langle \Delta Z_z^\mp(\tau) \sum_i [\Delta Z_i^\pm(\tau)]^2 \right\rangle \\ &= 4\epsilon^\pm V \tau \cos(\Theta_{BR}) \end{aligned} \quad (4.14)$$

where ΔZ_z^\mp is the measure of fluctuations parallel to the mean field.

4.3 Analysis

This project uses ACE data [42, 58] from 1998 through 2005 and applies the above expressions of Kolmogorov's 4/5 law and its isotropic, 1D, and 2D MHD analogues to the solar wind. The merged MAG and SWEPAM data has a resolution of 64 seconds. Data is stored in solar rotation files and in our analysis we break each 28 day solar rotation into fourteen two-day subintervals. Each two day interval is treated as an independent set for which we compute the above cascade rates. The expression for the cascade rate involves the lag vector L and in order to combine statistics from different intervals with different wind speeds, it is necessary to use a common spatial grid. To solve this issue we interpolate the results from each two day subinterval onto a common length grid that is based on a 64 s data resolution and a 400 km/s flow speed. The resulting interpolated structure function estimates derived from each two day interval are then summed and the ensemble average is obtained by dividing the sum by the total number of estimates at each lag value. In the case of one- and two-dimensional MHD geometries, we rotate the Elsässer variables into mean-field coordinates [5, 6], so it is necessary to have a well-defined mean field direction. The use of two-day subintervals allows for this specification. We also use the mean density from each 2-day interval. This work experimented with various additional data selection and processing mechanisms that are explained in the appendix, but we ultimately decided not to use them.

From the perspective of solar wind physics the distinction between Elsässer variables Z^+ and Z^- , which describe propagation parallel or anti-parallel to the mean magnetic field, can be made more significant by considering the direction of the mean field. In the solar wind the key distinction is outward vs. inward propagation with outward propagation generally dominating the data at 1 AU [5, 54]. We use the mean radial orientation of the magnetic field in a two day interval and the conversion between Z^\pm and $Z^{in/out}$ to rewrite eq. (4.8)–(4.14) as:

$$ISO D_3^{in/out}(\tau) \equiv \left\langle \Delta Z_R^{out/in}(\tau) \sum_i [\Delta Z_i^{in/out}(\tau)]^2 \right\rangle$$

$$= (4/3)\epsilon^{in/out}V\tau, \quad (4.15)$$

$$\begin{aligned} {}^{2D}D_3^{in/out}(\tau) &\equiv \left\langle \Delta Z_y^{out/in}(\tau) \sum_i [\Delta Z_i^{in/out}(\tau)]^2 \right\rangle \\ &= 2\epsilon^{in/out}V\tau \sin(\Theta_{BR}), \end{aligned} \quad (4.16)$$

$$\begin{aligned} {}^{1D}D_3^{in/out}(\tau) &\equiv \left\langle \Delta Z_z^{out/in}(\tau) \sum_i [\Delta Z_i^{in/out}(\tau)]^2 \right\rangle \\ &= 4\epsilon^{in/out}V\tau \cos(\Theta_{BR}). \end{aligned} \quad (4.17)$$

With these modifications in the analysis, and binning each two day estimate of the structure functions accordingly, we are able to separately determine the cascade rate for fluctuations traveling toward and away from the sun.

4.3.1 All Data

Figure 4.1 displays the results of applying the above formalism to seven years of ACE data. The analysis described here forms the basis for all that follows in this paper. The trace of the second order structure function for the Elsässer variables

$$S_2(\tau) \equiv \left\langle \sum_i [Z_i(t+\tau) - Z_i(t)]^2 \right\rangle \quad (4.18)$$

can then be used to estimate the trace of the autocorrelation matrix

$$R(\tau) \equiv \sum_i \langle Z_i(t+\tau)Z_i(t) \rangle \quad (4.19)$$

under the assumption of homogeneity [57]

$$R(\tau) = \delta B_{rms}^2 - S_2(\tau)/2. \quad (4.20)$$

For data intervals of this size with a maximum lag bordering on the correlation time it is possible to estimate δB_{rms}^2 from the value of S_2 at maximum lag. The trace of the power spectrum can then be computed from R^\pm in the usual manner. Figure 4.1 (top right) shows the resulting power spectra for outward propagation (blue) and inward propagation (red) with the solid black line giving the average, or total, power. We can use equation 4.1 to estimate the average energy cascade rate at 1 AU according to the computed average power spectrum. A best fit power law index for the total MHD power spectrum in Figure 4.1 is $q = -1.6 \pm 0.15$, which is $\frac{1}{2}\sigma$ from the Kolmogorov [28] prediction for isotropic turbulence. Table 4.1 lists the best-fit power law indexes for all spectra shown in this paper. In every instance examined here the power law index of the spectra of Z^{out} , Z^{in} , and the total are consistent with $-5/3$. Fitting of eq. (4.2) for this same spectrum yields $\epsilon_P = 5.5 \times 10^4$ Joules/kg-s which is greater than the observed radial dependence of the thermal proton temperature will allow. Moreover, this heating rate will result in the thermal proton temperature increasing with heliocentric distance.

Figure 4.1 shows that outward propagating fluctuations are energetically dominant in this sample, as expected. This asymmetry between outward and inward propagation suggests that we use the generalized Kolmogorov phenomenology of eq. (4.5). Applying this formalism to Figure 4.1 yields $\epsilon_P^{out} = 2.5 \times 10^4$ Joules/kg-s and $\epsilon_P^{in} = 1.2 \times 10^4$ Joules/kg-s and the total

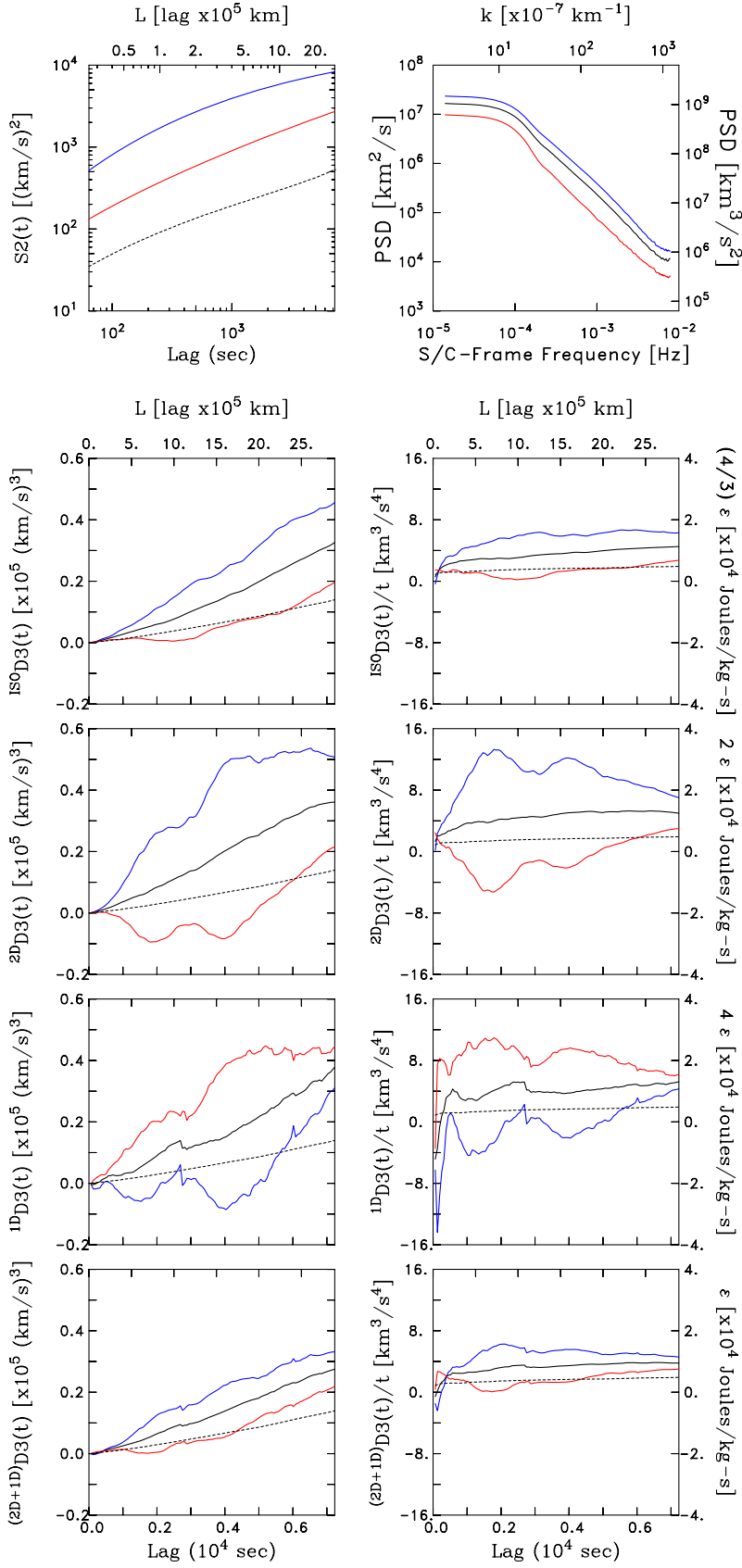


Figure 4.1: Lifetime analysis using ACE data from 1998–2004. Top panels show S_2 and resulting power spectra for outward (blue) and inward (red) propagating MHD. Solid black line gives average MHD. Dashed black line gives hydrodynamic value. Left/right shows D_3 and ϵ for top/down isotropic, 2D, 1D and 2D+1D sum.

Table 4.1: Computed power law index from power spectra.

Figure	$q \pm \sigma_q$ (Stand. Dev.)		
	MHD Total	MHD Outward	MHD Inward
Fig. 4.1	-1.60 ± 0.15 (0.48)	-1.62 ± 0.05 (0.14)	-1.56 ± 0.05 (0.17)
Fig. 4.2	-1.61 ± 0.06 (0.20)	-1.63 ± 0.06 (0.20)	-1.60 ± 0.05 (0.17)
Fig. 4.3	-1.61 ± 0.06 (0.18)	-1.63 ± 0.06 (0.20)	-1.55 ± 0.08 (0.26)
Fig. 4.4	-1.59 ± 0.07 (0.21)	-1.65 ± 0.08 (0.25)	-1.54 ± 0.08 (0.25)
Fig. 4.5	-1.76 ± 0.07 (0.22)	-1.72 ± 0.09 (0.28)	-1.78 ± 0.09 (0.27)

cascade rate $\epsilon_P^T = (\epsilon_P^{out} + \epsilon_P^{in})/2 = 1.8 \times 10^4$ Joules/kg-s. Note that we retain the subscript “P” because these estimates are derived exclusively from the power spectra. All estimates for ϵ derived from the power spectra alone are listed in Table 4.2. Again, this estimate for the total heating rate is too large. Note that neither of these three expressions is capable of accounting for a negative cascade rate on any component of the turbulence.

The plot $^{ISO}D_3(\tau)$ derived from eq. (4.15) displays the results of applying the structure function equations 4.6 and 4.7 to seven years of ACE data, and to its right $^{ISO}D_3(\tau)/\tau$ is the result of the division by the time lag. The rate of dissipation per unit mass for outward (blue) and inward (red) propagating waves, the total rate of dissipation (solid black), and the hydrodynamic estimate (dashed black) can all be derived from this plot. The outward traveling waves are more aggressively damped than those traveling inward. $^{2D}D_3(\tau)$ derived from eq. (4.16) is an analysis of the 2D and hydrodynamic expressions and $^{2D}D_3(\tau)/\tau$ is the rate of turbulent dissipation per unit mass assuming a 2D geometry with k -vectors perpendicular to the mean field direction. Outward flowing disturbances (blue) again produce a higher rate of dissipation than their inward flowing counterparts (red). The solid black line again shows the total heating rate, while the dashed black line is derived from the hydrodynamic approximation eq. (4.6), which is the same for all panels in this figure. $^{1D}D_3(\tau)$ shows the 1D geometry result according to eq. 4.17 and $^{1D}D_3(\tau)/\tau$ is the ensuing plot for the rate of energy cascade along the mean-field direction. The same color scheme is employed and it is worthy to note the reversal of roles between the rate of dissipation corresponding to outward- and inward-traveling waves as the inward-moving disturbances now have a higher associated rate of dissipation.

Table 4.2: Energy cascade rates computed from power spectra.

Figure	$\epsilon \pm \sigma_\epsilon$ (Stand. Dev.) [$\times 10^3$ Joules/kg-s]			
	ϵ_P	ϵ_P^{out}	ϵ_P^{in}	ϵ_P^T
Fig. 4.1	55.34 ± 1.52 (4.82)	25.19 ± 0.65 (2.06)	11.76 ± 0.37 (1.16)	18.47 ± 0.37 (1.18)
Fig. 4.2	22.82 ± 0.62 (1.95)	11.22 ± 0.27 (0.87)	6.46 ± 0.15 (0.47)	8.84 ± 0.16 (0.49)
Fig. 4.3	126.00 ± 3.90 (12.34)	54.80 ± 1.55 (4.90)	23.42 ± 0.86 (2.73)	39.11 ± 0.89 (2.81)
Fig. 4.4	10.00 ± 0.15 (0.46)	5.02 ± 0.08 (0.24)	3.28 ± 0.07 (0.21)	4.15 ± 0.05 (0.16)
Fig. 4.5	82.27 ± 3.16 (9.99)	40.93 ± 1.58 (5.00)	33.75 ± 1.25 (3.95)	37.34 ± 1.01 (3.19)

Table 4.3: Computed energy cascade rates for all D_3 in Figure 4.1.

Geometry	$\epsilon \pm \sigma_\epsilon$ (Stand. Dev.) [$\times 10^3$ Joules/kg-s]			
	MHD Outward	MHD Total	MHD Inward	Hydrodynamic
ISO	$10.50 \pm 0.22(2.39)$	$6.50 \pm 0.14(1.45)$	$2.50 \pm 0.12(1.26)$	$4.96 \pm 0.07(0.76)$
2D	$12.16 \pm 0.29(3.12)$	$5.63 \pm 0.10(1.10)$	$-0.91 \pm 0.27(2.92)$	$4.96 \pm 0.07(0.76)$
1D	$-0.23 \pm 0.17(1.82)$	$2.48 \pm 0.08(0.88)$	$5.19 \pm 0.10(1.09)$	$4.96 \pm 0.07(0.76)$
2D+1D	$11.93 \pm 0.34(3.61)$	$8.11 \pm 0.17(1.85)$	$4.28 \pm 0.21(2.20)$	$4.96 \pm 0.07(0.76)$

Politano and Pouquet [51] left the dimension of the turbulence as an open variable, although they did derive the isotropic case as an example. Our eq. (4.13), (4.14), (4.16) and (4.17) assumed one and two dimensional geometries in acknowledgement of the *Matthaeus et al.* [39], *Bieber et al.* [6] and *Dasso et al.* [13] analyses. The third order structure function for the composite 2D+1D geometry

$$^{2D+1D}D_3(\tau) = (1/2)^{2D}D_3(\tau) + (1/4)^{1D}D_3(\tau) \quad (4.21)$$

then allows us to compute $^{2D+1D}D_3(\tau)/\tau$ which is the calculated rate of energy dissipation per unit mass for this composite geometry. Figure 4.1 shows the result of this analysis where outward propagating waves (blue) again dominate over those traveling inward (red). It is interesting to note that this result agrees very well with the isotropic calculation. A tabulation of the calculated rates of energy dissipation for all geometries and directions can be found in Table 4.3.

The above treatment of the solar wind has flaws in that it assumes a direction of k for each of the 2D and 1D geometry calculations. The analysis does not reliably separate parallel and perpendicular wave vectors, thereby risking double counting and misidentification. To solve these issues we adapt the treatment used by *Dasso et al.* which employs a division of the solar wind into high and low speed categories. With this separation we can now apply eq. (4.16) and (4.17) reliably.

4.3.2 High and Low Wind Speed

In our analysis the classification of the slow solar wind is a two day interval for which the average flow speed is below 400 km/s, a classification consistent with *Dasso et al.*. The results of Dasso et al. demonstrate a dominant k -vector perpendicular to the mean field in the low speed solar wind. For this reason we treat the low speed wind with an assumed 2D geometry. The top panel of Figure 4.2 shows the trace of the second order structure function from which the trace of the power spectrum (PSD) is computed. The same color scheme is employed here where the blue line denotes the power associated with outward propagation, the red line is the power of inward propagation, and the solid black line gives the total power contained within the spectrum. From the power spectrum, we can extract an estimate for the rate of energy dissipation per unit mass, $\epsilon_P = 2.3 \times 10^4$ Joules/kg-s which is again too large and would result in thermal proton temperatures increasing with heliocentric distance. Using the generalized Kolmogorov phenomenology of eq. 4.5 we get a total heating rate of $\epsilon_P^T = 8.8 \times 10^3$ Joules/kg-s which is marginally in agreement with expectations.

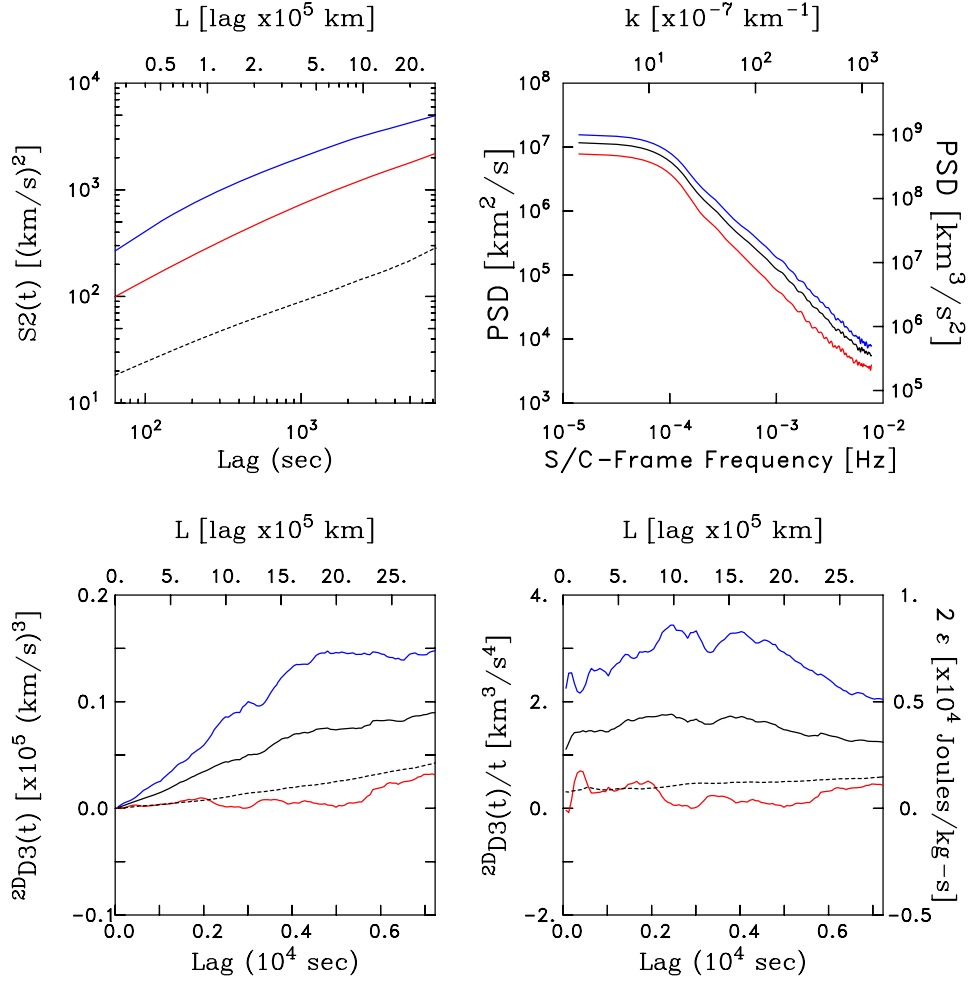


Figure 4.2: Second-order structure function, S_2 for $V_{SW} < 400$ km/s. Power spectral density, PSD, computed from S_2 . D_3 computed for 2D component perpendicular to mean field. Resulting energy cascade rate computed from the 2D formalism.

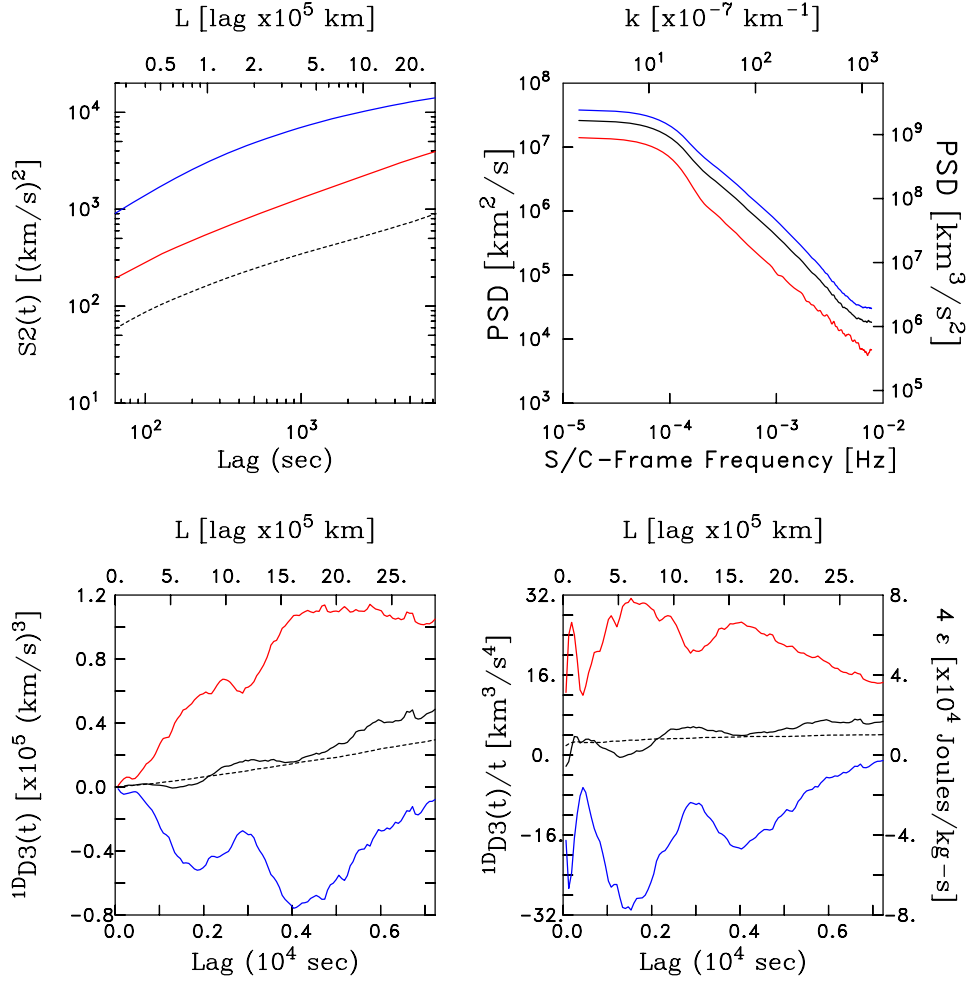


Figure 4.3: Second-order structure function, S_2 for $V_{SW} > 500$ km/s. Power spectral density, PSD, computed from S_2 . D_3 computed for 1D component parallel to mean field. Resulting energy cascade rate computed from the 1D formalism.

${}^{2D}D_3(\tau)$ is the resulting plot from the application of eqn. 4.16 to low speed intervals of data. The bottom panel of figure 4.2 shows the cascade rate per unit mass of the slow solar wind as a function of lag. The outward-traveling fluctuations are again transferring energy to small scales more strongly than fluctuations traveling toward the sun. The resulting total for the energy cascade rate derived from structure functions for the 2D geometry is $\epsilon^T = 1.9 \times 10^3$ Joules/kg-s which is very consistent with the local gradient in proton temperature.

The classification of the fast solar wind is any interval with an average speed above 500 km/s. *Dasso et al.* show a highly one-dimensional turbulence geometry oriented along the mean magnetic field direction for high speed streams. As a result, we apply eqn. 4.17 to the fast solar wind. Figure 4.3 is a result of the high wind speed selection process. The top two panels show the trace of the second order structure function (S_2) and the ensuing power spectrum from which we extract a heating rate of $\epsilon_P = 1.3 \times 10^5$ and $\epsilon_P^T = 3.9 \times 10^4$ Joules/kg-s, both of which are much too large.

${}^{1D}D_3(\tau)$ is an application of eqn. 4.17 to the fast solar wind. ${}^{1D}D_3(\tau)/\tau$ is the calculated cascade rate for the fast solar wind. Figure 4.1 applies these formalisms to the fast wind. Here the inward traveling fluctuations show a stronger cascade to small scales than those fluctuations propagating away from the sun with the majority component of outward propagating fluctuations experiencing negative cascade rates or spectral transfer to larger length scales away from the dissipation mechanism. This may be a form of selective decay or dynamic alignment acting on the field-aligned wave vectors. The resulting total energy cascade rate to small scales derived from structure functions for the 1D geometry is $\epsilon^T = 2.7 \times 10^3$ Joules/kg-s which is again very consistent with the local gradient of proton temperatures. Table 4.4 displays the computed cascade rates for slow and fast solar wind derived from the structure function methods.

4.3.3 Minority Components

The above analysis of the turbulence in high- and low-speed streams focused on the majority components; k -vectors along the mean field direction in the fast wind and k -vectors perpendicular to the mean field in the slow wind. We will now consider the minority component in both the high- and low-speed solar wind by selecting intervals in the correct range of wind speeds with mean fields suitably oriented to display a single component of the turbulence.

Figure 4.4 uses two day intervals with an average flow speed below 400 km/s and $0^\circ < \Theta_{BR} < 25^\circ$. By restricting data intervals to those with nearly radial mean fields we preferentially observe the field-aligned k -vectors while the perpendicular k -vectors are Doppler shifted to zero frequency. The top two panels of figure 4.4 show the trace of the second order structure function and the resultant power spectrum which yields heating rates of $\epsilon_P = 1.0 \times 10^4$, which is again too large, and $\epsilon_P^T = 4.2 \times 10^3$ Joules/kg-s, which is marginally acceptable if it were the total cascade rate for the turbulence. However, the latter value seems high for the cascade of the minority geometry alone.

${}^{1D}D_3(\tau)$ is a result of applying the 1D formalism of eq. (4.17) to the slow solar wind with radial mean fields. The division by lag results in ${}^{1D}D_3(\tau)/\tau$ and is a measure of the turbulent cascade rate of the minority component in the slow solar wind. The dominant outward-traveling fluctuations exhibit a stronger cascade to small scales than fluctuations traveling inward until the larger lag values at which point the inward-moving fluctuations produce a higher cascade rate. The total heating rate of 1.2×10^3 Joules/kg-s seems entirely

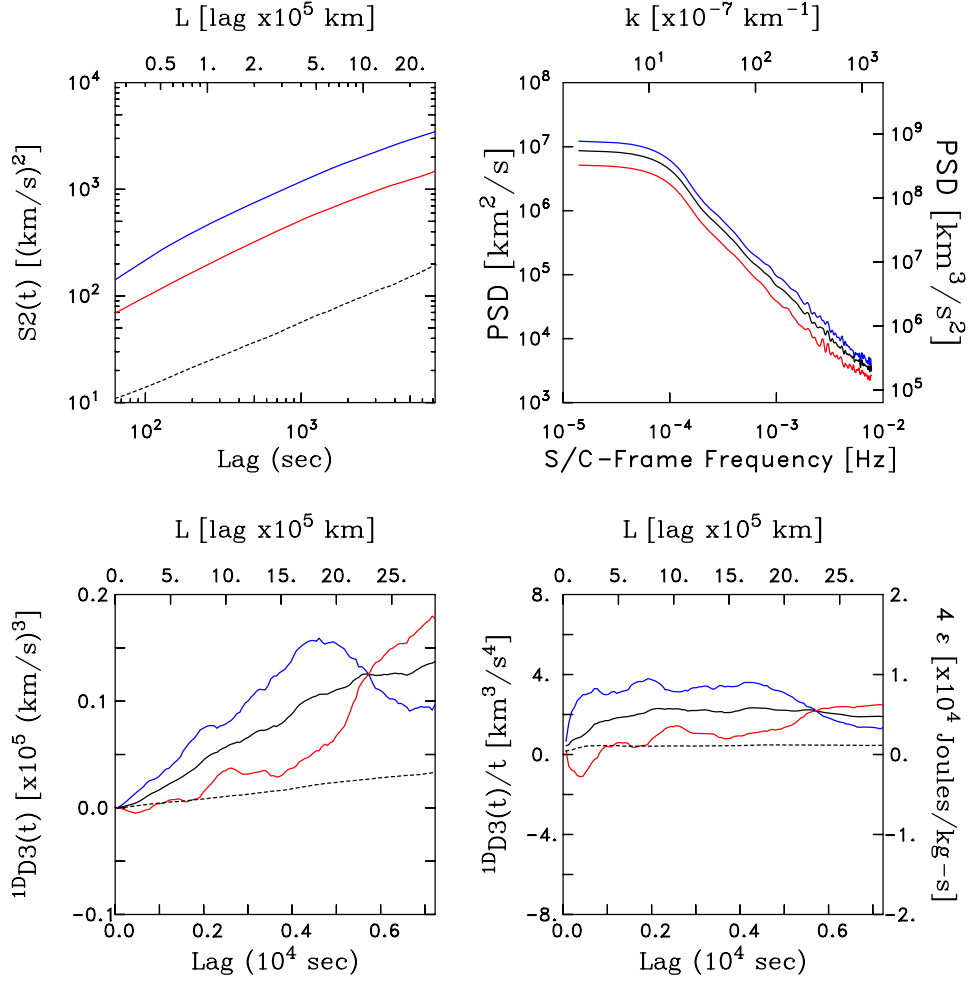


Figure 4.4: Same as Figure 4.3, but computed from data subset where $V_{SW} < 400$ km/s and $0^\circ < \Theta_{BR} < 25^\circ$.

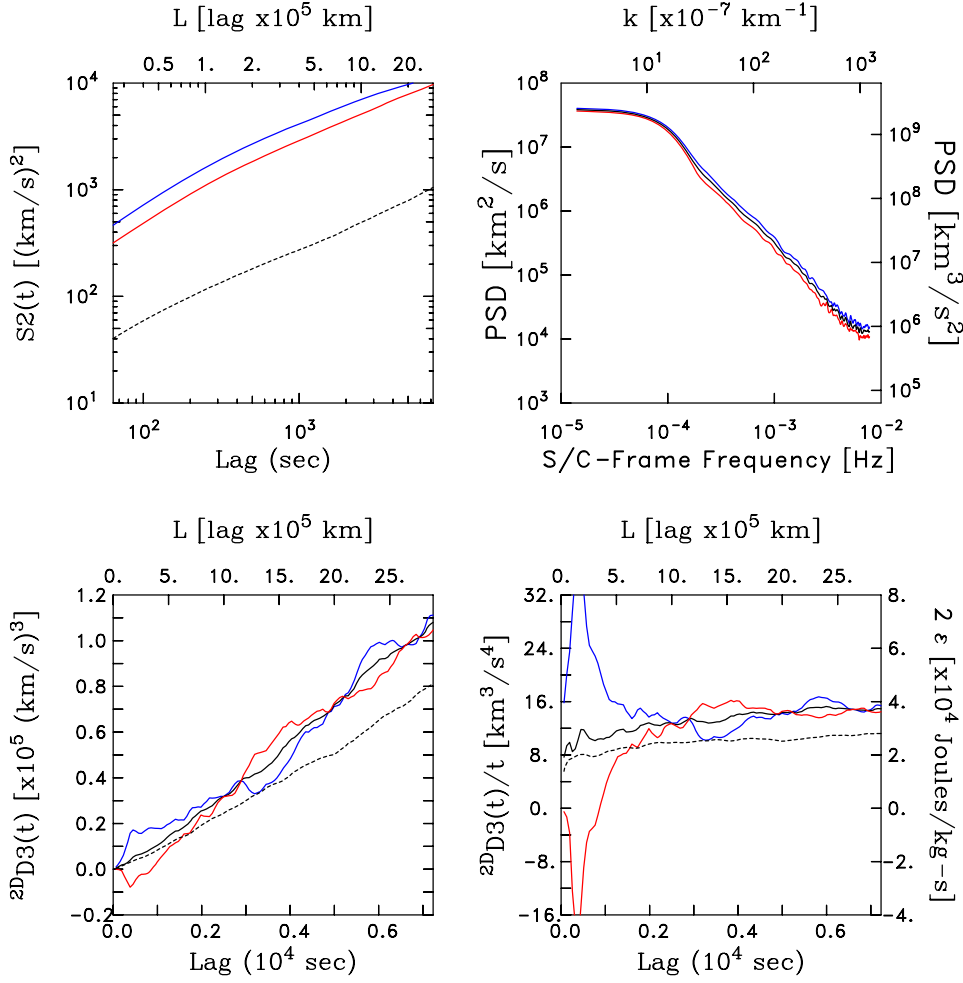


Figure 4.5: Same as Figure 4.2, but computed from data subset where $V_{SW} > 500$ km/s and $65^\circ < \Theta_{BR} < 90^\circ$.

plausible.

Figure 4.5 is an analysis of the minority component in the fast solar wind. The figure is composed of intervals with an average flow speed above 500 km/s and a magnetic field orientation $65^\circ < \Theta_{BR} < 90^\circ$. The top two panels show the trace of the second order structure function and the power spectrum. We extract dissipation rates of $\epsilon_P = 8.2 \times 10^4$ and $\epsilon_P^T = 3.7 \times 10^4$ Joules/kg-s from the power spectra and both values are too large. The power contained in the outward and inward modes are nearly indistinguishable.

With the line of sight confined to the plane perpendicular to the mean field direction, we examine the two-dimensional geometry described by eq. (4.16). The lower two panels show the 2D geometry results ${}^{2D}D_3(\tau)$ and ${}^{2D}D_3(\tau)/\tau$ derived from eq. (4.16). The heating rate of the outward-traveling fluctuations is only slightly larger than that for inward-propagating fluctuations, seemingly in keeping with the equality of the power spectra of the two components. The total heating rate of 1.6×10^4 Joules/kg-s is high, but in this instance may reflect a transient pulse as the system evolves toward two-dimensionality [19, 20, 40]. Table 4.4 displays the results of the energy cascade rate of the minority component in the fast and slow solar wind as derived from structure function methods.

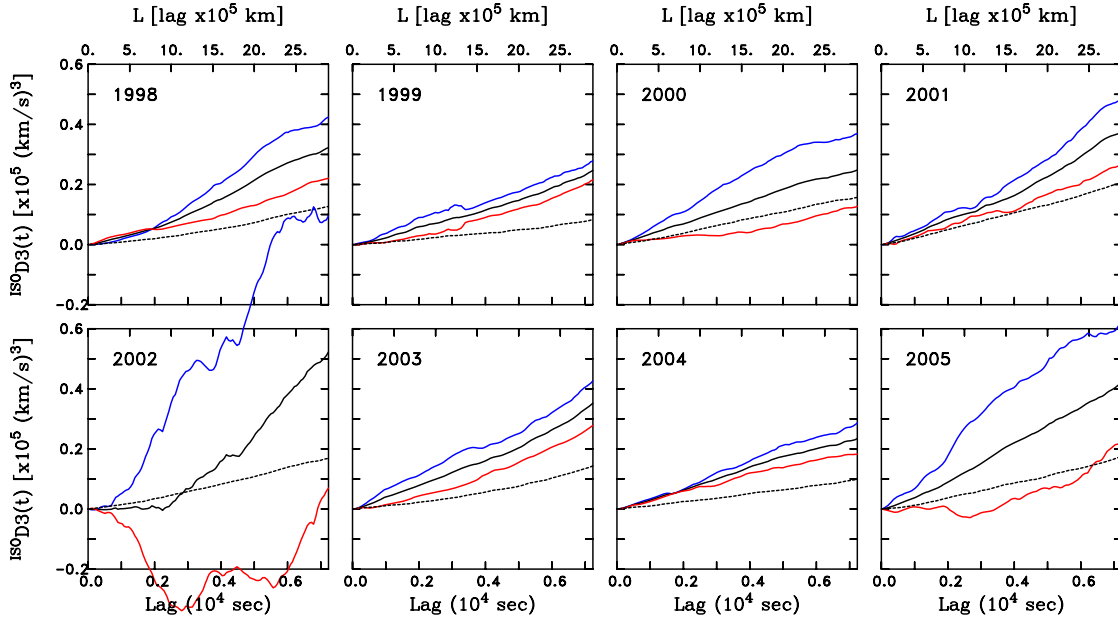


Figure 4.6: Yearly analysis of D_3 using isotropic formalism. Color convention holds.

4.3.4 Yearly Analysis

Figure 4.6 displays the results of applying eqn. 4.15 to each year of data from 1998 through 2005. This is the isotropic analysis which appears to give a good assessment of the average heating rate if one disregards the geometry issues. Table 4.5 lists the computed cascade rates for Figure 4.6 and these same average values are shown in Figure 4.7. Uncertainties are plotted in Figure 4.7, but are often smaller than the symbol used. We find that the outward-propagating component is energetically dominant every year and that this component possesses a more aggressive direct cascade to small scales than the minority inward-propagating component. No clear evidence of a solar cycle effect is seen. Some years (2002 and 2005) show strongly asymmetric cascade rates between the two components, but the total heating rate remains somewhere between $5 - 9 \times 10^3$ Joules/kg-s. This is the correct and expected range of values and the source of the extreme asymmetry some years is not well understood. The hydrodynamic expression eq. 4.6 given by the dashed line in Figure 4.7 consistently yields lower estimates for the cascade rate at $2 - 5 \times 10^3$ Joules/kg-s, which are themselves not unreasonable estimates.

Table 4.4: Computed energy cascade rates for high and low wind speeds, and their minority components in Figures 4.2, 4.3, 4.4, and 4.5.

Figure	$\epsilon \pm \sigma_\epsilon$ (Stand. Dev.) [$\times 10^3$ Joules/kg-s]			
	MHD Outward	MHD Total	MHD Inward	Hydrodynamic
Fig 4.2	$3.48 \pm 0.05(0.52)$	$1.90 \pm 0.02(0.21)$	$0.32 \pm 0.02(0.21)$	$1.44 \pm 0.02(0.24)$
Fig 4.3	$-8.69 \pm 0.48(5.14)$	$2.66 \pm 0.13(1.38)$	$14.00 \pm 0.29(3.04)$	$10.70 \pm 0.15(1.61)$
Fig 4.4	$1.76 \pm 0.05(0.49)$	$1.24 \pm 0.02(0.25)$	$0.72 \pm 0.05(0.57)$	$1.37 \pm 0.01(0.15)$
Fig 4.5	$19.54 \pm 0.61(6.53)$	$16.46 \pm 0.20(2.12)$	$13.39 \pm 0.88(9.34)$	$30.75 \pm 0.32(3.41)$

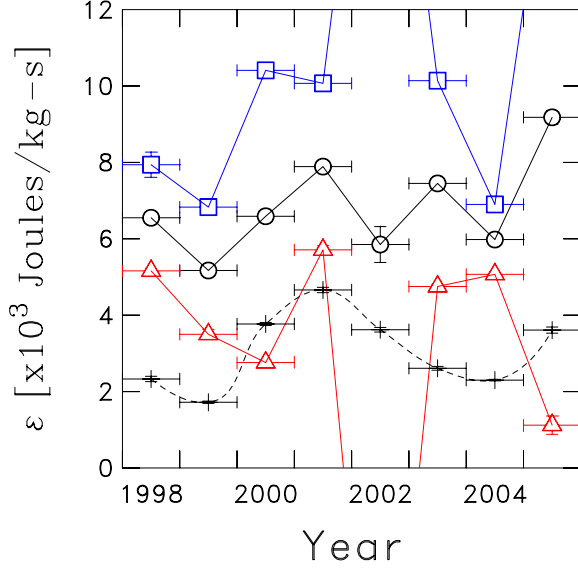


Figure 4.7: Summary of heating rates shown in Figure 4.6 and listed in Table 4.5. Color convention holds.

Table 4.5: Computed yearly energy cascade rates in Figure 4.6.

Year	$\epsilon \pm \sigma_\epsilon$ (Stand. Dev.) [$\times 10^3$ Joules/kg-s]			
	MHD Outward	MHD Total	MHD Inward	Hydrodynamic
1998	$7.94 \pm 0.33(3.53)$	$6.55 \pm 0.16(1.69)$	$5.16 \pm 0.07(0.75)$	$3.89 \pm 0.11(1.15)$
1999	$6.83 \pm 0.10(1.11)$	$5.17 \pm 0.10(1.01)$	$3.50 \pm 0.13(1.41)$	$2.87 \pm 0.04(0.44)$
2000	$10.41 \pm 0.13(1.40)$	$6.59 \pm 0.04(0.44)$	$2.76 \pm 0.07(0.73)$	$6.29 \pm 0.07(0.75)$
2001	$10.07 \pm 0.18(1.92)$	$7.89 \pm 0.13(1.34)$	$5.71 \pm 0.11(1.16)$	$7.77 \pm 0.11(1.17)$
2002	$21.94 \pm 0.85(9.05)$	$5.85 \pm 0.47(4.98)$	$-10.25 \pm 0.69(7.31)$	$6.03 \pm 0.10(1.08)$
2003	$10.14 \pm 0.18(1.88)$	$7.45 \pm 0.12(1.26)$	$4.75 \pm 0.15(1.57)$	$4.36 \pm 0.08(0.89)$
2004	$6.90 \pm 0.11(1.16)$	$5.98 \pm 0.08(0.80)$	$5.07 \pm 0.06(0.59)$	$3.84 \pm 0.03(0.28)$
2005	$17.24 \pm 0.23(2.45)$	$9.18 \pm 0.18(1.86)$	$1.12 \pm 0.24(2.56)$	$6.01 \pm 0.13(1.43)$

4.4 Summary

With growing evidence that a turbulent cascade provides the energy to heat the background plasma we have turned to the third-order structure function formalism of *Politano and Pouquet* [50, 51] in an effort to accurately resolve without heuristic assumption the rate of energy cascade through the inertial range. We have used the formalism of Politano and Pouquet to express structure function forms applicable to hybrid turbulent geometries where energy is distributed over wave vectors both parallel and perpendicular to the mean magnetic field and we gather our statistics according to inward and outward propagating fluctuations. We have shown that the above formalism works remarkably well and predicts a total energy cascade that is consistent with the local gradient of the proton temperature. We have shown that most often the energetically dominant, outward propagating component exhibits a stronger cascade to small scales than the minority, inward propagating component, which seems consistent with observations beyond 1 AU [54]. The exception to this is seen in field-aligned wave vectors within high-speed winds.

What is most significant in this work, apart from the demonstration that the inertial range cascade provides a measurable dynamic to bring $\langle \delta \mathbf{V} \cdot \delta \mathbf{B} \rangle \rightarrow 0$, is the unification of implied heating rates provided by large-scale transport theory [71, 70, 41], with that required of dissipation at the small scales of the dissipation range, and the heating rate inferred from the local gradient in proton temperature [65, 53]. This analysis accurately and objectively resolves the rate of energy cascade through the inertial range. It tracks the energy injected by the large-scale transients that are modelled by transport theory and measures the passage of energy through the intermediate scales of the inertial range as it cascades to the small scales for dissipation. As with *Vasquez et al.* [67] we have shown that the heuristic theories of cascade rates based on power spectrum levels fails in this regard by consistently predicting cascade rates that are too large.

4.5 Detrending and Stationarity

There is a philosophical distinction in the data that is difficult to address objectively: Are transients and various disturbances of a solar source part of the turbulence we wish to study, or are they possible sources that are separate from the homogeneous turbulence concept? This question is made more compelling when one realized that a 100 km/s ramp in solar wind speed over the course of 24 hours, which is a common and rather benign observation, is comparable to the signal we extract in the analysis. The general rotation of the IMF within a magnetic cloud has a similar effect. If these represent shears in the flow, then they are sources of the turbulence and should be included in this analysis. If they are converging flows or ideal rotations without local gradients, then it is less clear what their role is locally in the generation of turbulence.

The focus of the study is to analyze the in situ dynamics of the turbulence and not the large-scale structures that drive the turbulence, and so we attempted to filter through the intervals and only use those that pass our tests. We made attempts to remove such signals from the data with a combination of detrending and stationarity testing [35]. We found no significant or consistent change in the results, except in the general decrease of statistical significance that comes with a reduction in the ensemble size. For this reason, we choose not to employ such methods here and present the results of the simpler analyses that use all data subject to selection criteria listed in the text. Under this assumption, all

transients contribute to the interplanetary turbulence and with enough distinct contributions the ensemble includes all possible observations. This seems to be both the most reliable approach and philosophically the most appropriate since at 1 AU the sun's activity remains a major source of energy driving the turbulence.

4.6 Code Testing

Because the results for the k_{\parallel} cascade are unexpected and strongly indicate that the majority component of outward propagating fluctuations are enhanced through the cascade of the minority inward-propagating component, we should describe how the code was tested. Ordinarily, one would test codes of this type by building a synthetic data set with known properties that closely resembles the statistics of the measured variables. In this case, it is very difficult to build synthetic data with known and nontrivial S_3 properties that still closely mimic other aspects of interplanetary data (S_2 , $\langle \delta V \cdot \delta B \rangle$, etc.). After many attempts we realized that this was not necessary to testing the code we developed here and that all that is needed is to create a time series of known properties and predictable conclusions. We did this by first creating a time series for magnetic components $B(i) = i$ and velocity components $V(i) = \frac{1}{2}i$ with $4\pi\rho = 1$. Each component of B has the same value and likewise, each component of V is the same. These time series bear little resemblance to reality, but they do lead to predictable and testable conclusions. They yield $Z^+ = \frac{3}{2}i$ and $Z^- = \frac{1}{2}i$ so that $S_2^+(L) = \left(\frac{3}{2}L\right)^2$, $S_2^-(L) = \left(\frac{1}{2}L\right)^2$, $^{ISO}D_3^+(L) = \left(\frac{1}{2}L\right) 3 \left[\left(\frac{3}{2}\right)L\right]^2$, and $^{ISO}D_3^-(L) = \left(\frac{3}{2}L\right) 3 \left[\left(\frac{1}{2}\right)L\right]^2$. Similar results can be obtained for the 2D and 1D formalisms. This permits end-to-end testing of the codes with a high degree of validation. Later tests can relax aspects of test conditions as warranted.

Chapter 5

Turbulence of the Inner Heliosphere

5.1 Anisotropic Turbulence in the Solar Wind

Up to this point this thesis has dealt with properties and measurements in the inertial range of the solar wind. Recalling the model of energy transfer in the solar wind discussed in Chapter 3, we can trace the cascade of energy from large scales of the energy-containing range through the intermediate scales of the energy-conserving inertial range into the small scales of the dissipation range where the fluid energy is converted to heat. Chapter 4 provides a quantitative description of the rate at which the energy cascades through the inertial range.

We focus here on the results of *Leamon et al.* [31], *Smith et al.* [61], and *Hamilton et al.* [22] who studied properties of solar wind turbulence at 1 AU in the high frequency end of the inertial range. *Smith et al.* study the magnetic variance anisotropy (the ratio of magnetic fluctuations perpendicular to the mean magnetic field to fluctuations parallel to the mean field) and find it scales with both proton beta and the amplitude of the power spectrum. In their analysis they also plot proton beta against the amplitude of the power spectrum of magnetic field oscillations and find them to be correlated, which leads to the result that magnetic variance anisotropy scales with both quantities. Proton beta is a unitless quantity defined as the ratio of thermal to magnetic energy density, and if the variation of the magnetic field is related to the proton temperature [61] it will be difficult to discern whether the anisotropy arises due to the variation of the proton beta or the amplitude of the power spectrum.

Leamon et al. and *Hamilton et al.* study the wave vector anisotropy in the solar wind by applying the *Bieber et al.* [6] method. This method of analysis is based on the ratio of power spectra in the x- and y-directions in mean field coordinates as defined by *Belcher and Davis* [5] where $\hat{z} \equiv \mathbf{B}/|\mathbf{B}_0|$ is the unit vector in the direction of the mean magnetic field, $\hat{y} \equiv -(\hat{z} \times \hat{R})/|(\hat{z} \times \hat{R})|$ where \hat{R} is the radial direction and is assumed to be the direction of the solar wind flow, and $\hat{x} \equiv \hat{y} \times \hat{z}$. The wave vector anisotropy gives an estimate of the relative energy contained in the fluctuation vectors perpendicular and parallel to the mean magnetic field. *Bieber et al.* determined that approximately 80% of the energy is contained in the 2D plane perpendicular to the magnetic field. *Leamon et al.* [31] apply the same analysis to observations in the inertial range at 1 AU and find 89% of the energy to reside in the perpendicular component. *Hamilton et al.* use the same analysis in both the inertial and dissipation ranges at 1 AU, but with an additional wind speed selection criteria. Their results demonstrate a nearly equal division of energy between wave vectors perpendicular and parallel to the mean field with no dependence of wave vector anisotropy on wind speed.

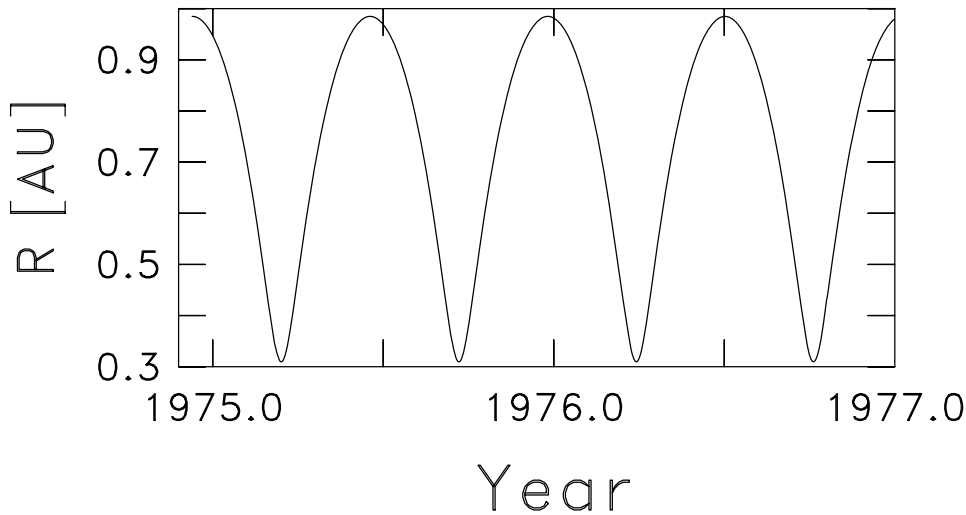


Figure 5.1: Heliocentric distance for Helios1 during years when data for this study was obtained.

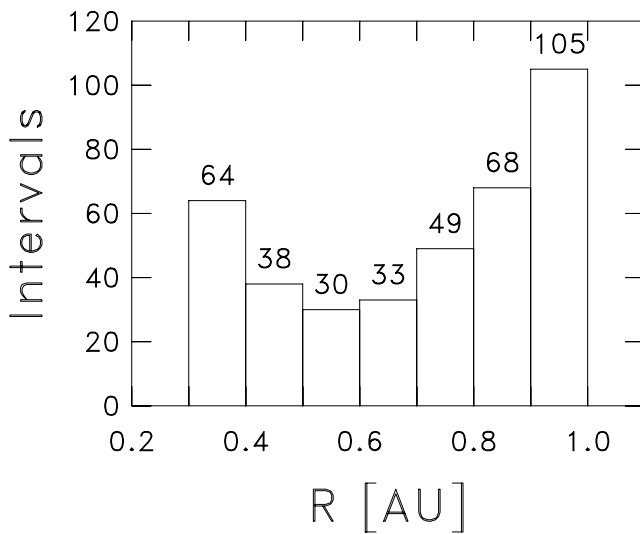


Figure 5.2: Number of intervals selected for study in increments of 0.1 AU.

In this analysis we extend the methods that have been used previously at 1 AU to the inner heliosphere with the Helios spacecraft. We analyze the magnetic variance and wave vector anisotropies as a function of both wind speed and heliocentric distance. We attempt to determine whether there is an observed spatial evolution of these turbulent properties as a function of heliocentric distance and whether there is a distinction between high and low wind speeds.

5.2 Helios Analysis

In the analysis we use Helios spacecraft magnetic field data from late 1974 through 1977 with 6 second resolution. The Helios spacecraft traversed an orbit with a perihelion of 0.3 AU and an aphelion of 1 AU, so the data spans this range as well. Figure 5.1 displays the heliocentric distance of the Helios spacecraft from 1974 until 1977. We use over 380 hand-

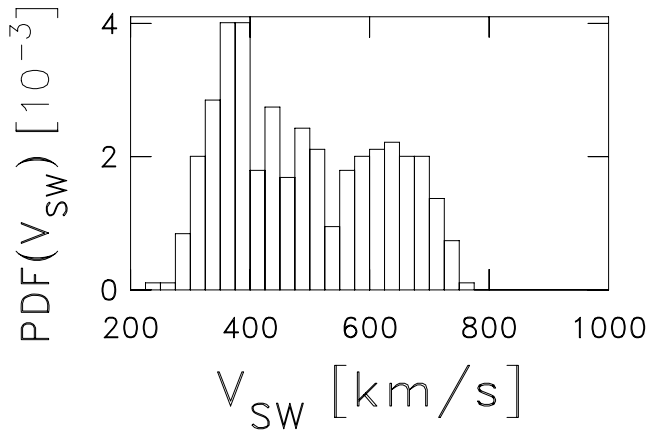


Figure 5.3: Distribution function of events according to wind speed.

selected stationary intervals ranging from four to six hours in length to create magnetic power spectra by the *Blackman and Tukey* [8] method with autocorrelation functions. Intervals with a defined power-law index through the inertial range were kept, and intervals without a power-law index were discarded. Intervals were chosen on the basis of providing a wide range of properties to analyze. In particular, we made sure to include intervals spanning the inner heliosphere down to 0.3 AU, and to choose intervals with both a high and low average solar wind velocity. Figure 5.2 displays the number of intervals chosen as a function of distance from the sun in increments of 0.1 AU, and Figure 5.3 is a probability distribution function of events selected as a function of average solar wind speed. These two plots demonstrate a full coverage of the inner heliosphere down to 0.3 AU and a range of wind speeds from 250 – 750 km/s.

In order to be able to select intervals based on stationarity, wind speed, and heliocentric distance, I first needed to convert raw data files into data plots. This process required that I learn a programming language with plotting capabilities. I have used the scientific computing languages of FORTRAN and C, but neither of these have the ability to create figures. To solve this problem I learned enough commands in the Interactive Data Language (IDL) to adapt codes written by R.J. Leamon for the study of ACE measurements so they would be able to plot Helios spacecraft observations. Once the Helios measurements were plotted, I could then choose the intervals and create magnetic power spectra. From the power spectra we analyze two intervals in the inertial range. The frequency ranges we used are from 5×10^{-3} to 2×10^{-2} Hz and from 3×10^{-2} to 7×10^{-2} Hz, which we refer to as the low and high frequency intervals respectively. The two parameters of the solar wind turbulence we examine are the magnetic field variance and wave vector anisotropies.

5.3 Magnetic Variance of the Inner Heliosphere

The magnetic field variance anisotropy is the ratio of magnetic fluctuations perpendicular to the mean magnetic field to the fluctuations parallel to the mean field. As stated in the introduction, *Smith et al.* [61] found variance anisotropy to scale with both proton beta (β_p) and the amplitude of the spectrum of magnetic fluctuations ($\delta B/B_0$). This result was the product of an analysis based on measurements taken with the ACE spacecraft at 1 AU and we seek to extend this analysis to the inner heliosphere as near to the sun as 0.3 AU

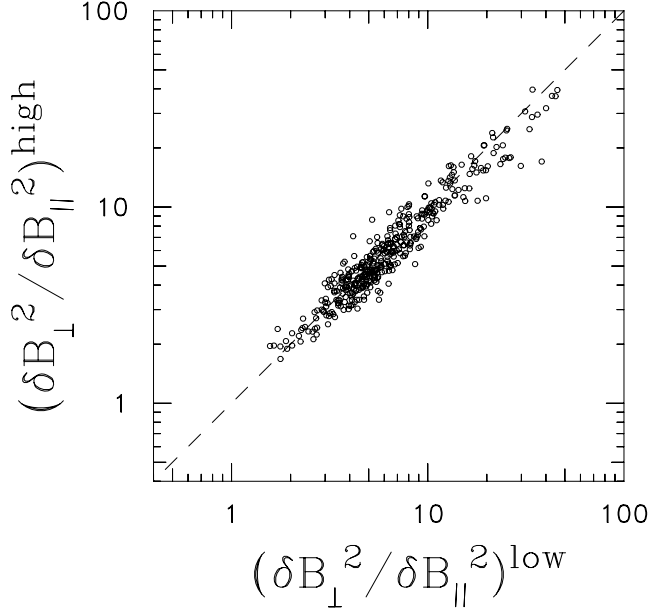


Figure 5.4: Scatter plot of variance anisotropy for high frequency range (side axis) vs. low frequency range (bottom axis) using all data.

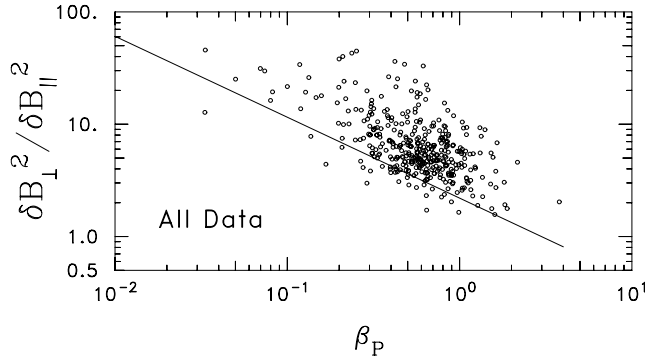


Figure 5.5: Scatter plot of variance anisotropy (side axis) for low frequency range vs. thermal proton β_p (bottom axis) for all data.

with the Helios spacecraft. In our analysis we measure the magnetic variance anisotropy in both the high and low frequency intervals. Figure 5.4 is a comparison of the variance anisotropy measured in the high frequency range plotted against the anisotropy measured for low frequencies. The dashed line shows equality and is provided as a reference. This figure displays a direct relationship between the two frequency ranges with perhaps a slightly stronger anisotropy in the low range at high values. This direct relationship implies that the anisotropy of the turbulence does not change as it travels through the inertial range. The higher anisotropy values in the low frequency range for strongly anisotropic events implies that such occurrences become less anisotropic at higher frequencies.

The magnetic variance anisotropy of the low frequency range is plotted against β_p in Figure 5.5. This plot is created using all of the intervals we analyzed with no selection based on heliocentric distance or wind speed. As in the case of *Smith et al.* we again find the variance anisotropy to scale with β_p . Figure 5.6 plots the magnetic variance anisotropy of the low frequency range against $\delta B/B_0$. The top panel of the figure uses all 387 intervals

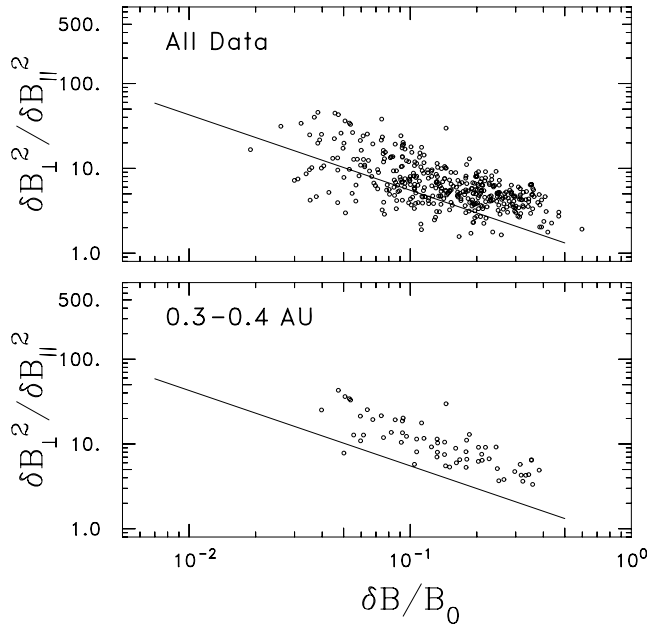


Figure 5.6: (top) Scatter plot of variance anisotropy for low frequency range (side axis) vs. integrated magnetic power normalized to mean field intensity (bottom axis) for all data. (bottom) Same for heliocentric distance range 0.3–0.4 AU.

from the Helios data base while the bottom panel uses only the 64 intervals in the 0.3–0.4 AU range. Both results show a scaling of the variance anisotropy with $\delta B/B_0$. This is again in accordance with the *Smith et al.* results at 1 AU. In fact, the trend line shown in Figures 5.5 and 5.6 is the same line used in the analysis at 1 AU. These results indicate that the magnetic variance anisotropy experiences no spatial evolution between 0.3 and 1 AU.

Similar to the results of *Smith et al.*, we again find a dependence of the magnetic variance anisotropy on both the proton beta and the amplitude of the power spectrum of magnetic fluctuations. Prior to the analysis we thought taking samples from varying heliocentric distances might break the correlation between the dependence on both β_p and $\delta B/B_0$ to determine which quantity is fundamental to the variance anisotropy, but this did not happen. Variance anisotropy scales with both quantities all the way down to 0.3 AU. Figure 5.7 plots the thermal energy of the protons in the solar wind against the amplitude of the power spectra and they are shown to be correlated. This correlation is what leads the magnetic variance anisotropy to scale with both parameters in Figure 5.7.

5.4 Spatial Evolution of the Power Spectral Index

The intervals included in this analysis were chosen on the basis of having a well-defined power law index. That is, on a log-log plot of the power spectrum of magnetic fluctuations as a function of frequency, all intervals are easily fit with a straight line within the inertial range. The power law index q is the slope of this straight line. In the turbulence described by Kolmogorov, the inertial range is characterized by a $-5/3$ power law index, but in our analysis we do not require intervals to have a $-5/3$ power law index so long as the index is well-defined. The power law index of the 387 intervals therefore experiences much variation. *Bavassano et al.* [3] demonstrate a dependence of the power law index in the inertial range

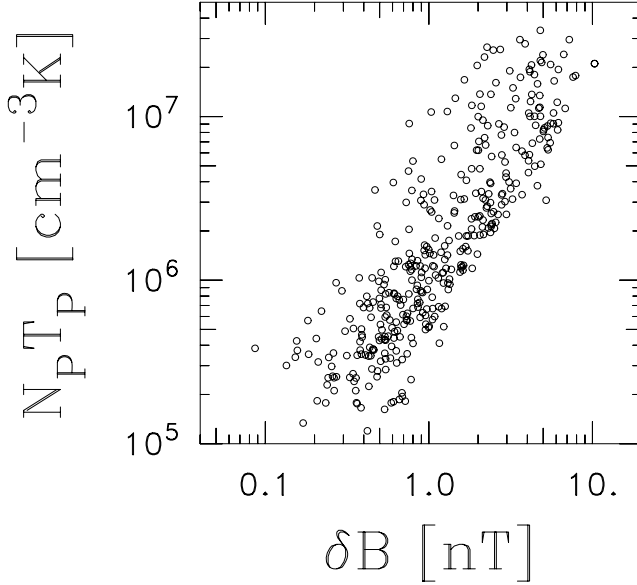


Figure 5.7: Scatter plot of proton thermal energy (side axis) vs. integrated magnetic fluctuation amplitude (bottom axis) for all data.

of solar wind fluctuations on the heliocentric distance. They show a steepening of the power spectra with increasing distance from the sun. Figure 5.8 plots the spectral index as a function of heliocentric distance in an attempt to confirm the results of *Bavassano et al.*. This figure contains results from both the high and low frequency intervals and analyzes all of the data in the top panel, high wind speed streams in the middle panel, and low speed streams in the bottom panel. Although the errors are rather large, to first order the spectral index of all data seems to show the same dependence on heliocentric distance as was shown by *Bavassano et al.*. The circular data point at the 1 AU value in all three panels is a result drawn from *Hamilton et al.* [22]. This plot is a source of concern and casts some doubt on the results that follow. The low frequency spectral indices hover around the $q = -1.6$ mark which is characteristic of Kolmogorov inertial range turbulence. The high frequency spectral indices, however, are much steeper around the $q = -1.8$ mark. The self-similar inertial range should not experience such a drastic change of power law index between two frequencies that lie securely within it. This result has made it necessary to run additional tests of the programs used in the analysis to ensure these results are physically significant and not a synthetic product of the codes.

5.5 Wave Vector Anisotropy of the Inner Heliosphere

As stated in the introduction, the test to find the orientation of the wave vectors in solar wind turbulence was developed by *Bieber et al.* [6] and its first application showed 80% of the energy exists in the 2D component perpendicular to the mean magnetic field. *Hamilton et al.* employed this same test and found a nearly equal mixture of wave vectors parallel and perpendicular to the mean magnetic field. Furthermore, *Hamilton et al.* selected events based on the average flow speed of the solar wind for each interval and found no distinction in wave vector orientation between the intervals with high speed ($V_{SW} > 500$ km/s) and low speed ($V_{SW} < 400$ km/s) streams. The method for determining the energy in the perpendicular

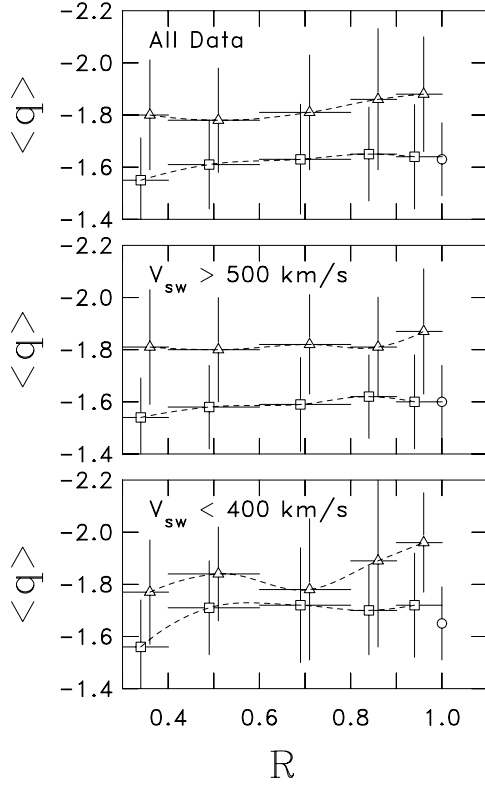


Figure 5.8: Means and variances of power law indexes for low frequency range (squares) and high frequency range (triangles) computed from all data (top), high speed wind intervals (middle) and low speed winds (bottom).

and parallel directions relies on the ratio of the power in the two components perpendicular to the mean field:

$$\frac{P_y}{P_x} = \frac{k_s^{1-|q|} + r' \left(\frac{2|q|}{1-|q|} \right) k_2^{1-|q|}}{k_s^{1-|q|} + r' \left(\frac{2}{1-|q|} \right) k_2^{1-|q|}} \quad (5.1)$$

where $k_2 = \frac{2\pi\nu}{V_{SW}\cos\Theta_{BR}}$ and $k_s = \frac{2\pi\nu}{V_{SW}\sin\Theta_{BR}}$, Θ_{BR} is the angle between the mean magnetic field and the flow direction of the solar wind, ν is the spacecraft frame frequency, r' is the energy in both the field aligned and perpendicular components, and $r = \frac{1}{1+r'}$ is the fraction of total energy in the field-aligned component. This explanation of the Bieber analysis is courtesy of *Smith et al.* [63].

Here we employ the Bieber test to examine the dependence of wave vector anisotropy on not only wind speed as demonstrated by *Hamilton et al.* but also on heliocentric distance. By using data from the Helios spacecraft we have the opportunity to compare the percentage of energy contained in the wave vectors perpendicular and parallel to the mean field at various locations in the inner heliosphere. By comparing results at different heliocentric distances it is possible to determine whether the wave vector anisotropy evolves as the solar wind expands from its solar source. Figure 5.9 displays the ratio of power in the two components perpendicular to the mean field as a function of the angle between the mean field and the solar wind flow direction Θ_{BR} . The minimum χ^2 fit of this plot gives an estimate of the percentage of energy contained in the field-aligned wave vector. All of the data ranging from heliocentric distances of 0.3 to 1 AU was used to create this figure with no selection based on wind speed. The top panel displays the results of the analysis in the low frequency

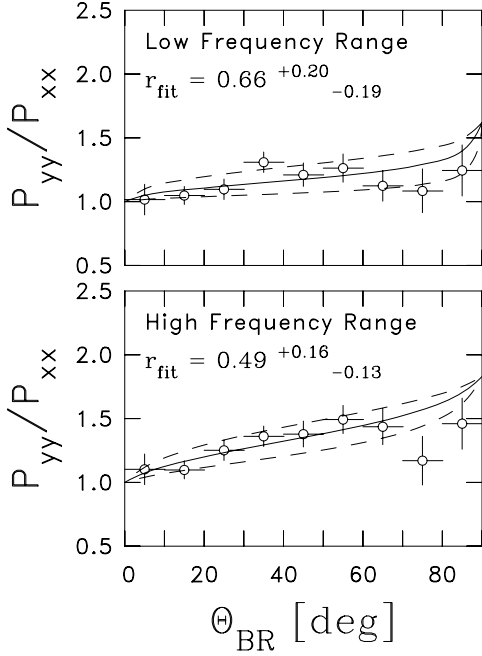


Figure 5.9: Distribution of computed ratio P_{yy}/P_{xx} binned by Θ_{BR} for all low frequency (top panel) and high frequency (bottom panel) data. Minimum χ_r^2 solution (solid line) and $\chi_r^2 + 1$ curves (dashed lines) are shown.

intervals and the bottom panel displays the results from the high frequency intervals. These results are dependent on the spectral index, and will change if Figure 5.8 changes. The dubious values of the spectral index lie in the high frequency range, and so it would be the bottom panel of Figure 5.9 that is likely to change if the spectral indices also change. As the plots stand, however, it appears that the low frequency interval contains a stronger percentage of field-aligned wave vectors than the high frequency interval. This implies that as the turbulent energy moves through the inertial range it becomes less field-aligned as the energy is transferred to the perpendicular 2D component.

Figure 5.10 displays the fraction of energy contained in the wave vectors aligned with the mean magnetic field as a function of heliocentric distance. The top panel of the figure displays results using all intervals, the middle panel selects for events with an average wind speed greater than 500 km/s, and the bottom panel includes only intervals with a wind speed below 400 km/s. Although the variance of the results is large (vertical lines), the percentage of energy contained in the wave vectors aligned with the mean magnetic field for both high frequency (triangles) and low frequency (squares) intervals appears to be independent of location in the inner heliosphere. The independence of heliocentric distance is particularly true in the top panel of Figure 5.10. The fast wind results seem to show a slight progression towards turbulence that is more highly aligned with the mean magnetic field as the distance from the sun increases, but the slow wind results show no real correlation with heliocentric distance. The high wind speed streams seem to show no more percentage of energy contained in the wave vector aligned with the mean magnetic field than the low wind speed streams. This is contrary to the results of *Dasso et al.* [2005] who showed the turbulence in the fast solar wind to be strongly one-dimensional in the direction parallel to the mean magnetic field, and the slow solar wind to be strongly two-dimensional in the plane perpendicular to the mean magnetic field. Similar to the results of this analysis, *Hamilton et al.* [22] also show

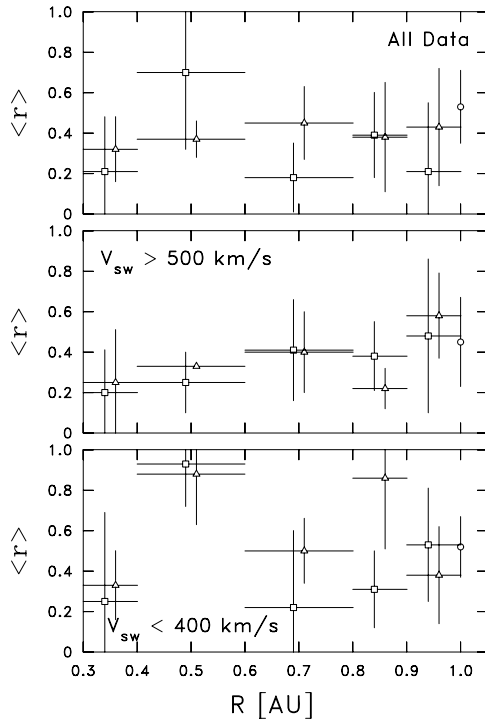


Figure 5.10: Means and variances of slab fraction for all wind speeds (top), high wind speeds (middle) and low wind speeds (bottom) for low frequency intervals (squares) and high frequency intervals (triangles).

no dependence of wave vector anisotropy on the solar wind speed. *Hamilton et al.* provide a resolution to these seemingly contradictory results. The resolution lies in the difference of frequencies used for the two analyses. *Hamilton et al.* show that $f_{sc} > 10^3$ Hz represents fluctuations that are too short-lived to be of solar origin and this holds down to the scope of the present analysis at 0.3 AU. All of our results arise from $f_{sc} > 10^3$ Hz whereas the work of Dasso et al. contains data from $f_{sc} < 10^3$ Hz. *Hamilton et al.* suggest that the two dimensional turbulence in slow wind streams and the one dimensional turbulence in the fast wind streams found by *Dasso et al.* could be a remnant of the solar source which does not appear at the high frequencies used in this study.

5.6 Conclusion

In this analysis we extend the findings of *Leamon et al.* [31], *Smith et al.* [61], and *Hamilton et al.* [22] to 0.3 AU. We extend the previous results based on observations made by the ACE and WIND spacecraft to observations made by Helios in an attempt to determine whether the properties of solar wind turbulence experience a spatial evolution between 0.3 and 1 AU. We have confirmed the results of Smith et al. made at 1 AU that the magnetic variance anisotropy scales with both proton beta and the amplitude of the power spectrum. Similar to their results, we were unable to break the correlation between the proton beta and the amplitude of the power spectrum. These results hold down to 0.3 AU, the closest to the sun Helios travels. Hamilton et al. found the wave vector anisotropy at 1 AU in the high frequency end of the inertial range to be independent of solar wind speed. We also analyze the high frequency end of the inertial range, but this analysis is not restricted to

measurements made at 1 AU, instead it includes measurements made in the range of 0.3 to 1 AU. We also find the wave vector anisotropy to be independent of solar wind speed. In addition, we find that there is no dependence of the wave vector anisotropy on heliocentric distance. These results of the magnetic variance and wave vector anisotropies that were made using data from the Helios spacecraft demonstrate that the turbulence measured at 0.3 AU is nearly identical to the turbulence at 1 AU. This implies that the turbulence in the solar wind is fully developed by the time it reaches 0.3 AU.

Chapter 6

Parting Remarks

When I began my academic career at the University of New Hampshire I had not the faintest idea of what the solar wind was. Over three years later, I am completing an honors thesis on the topic “Turbulence of the Solar Wind”. The journey has not been easy, but it has been enjoyable and I have learned a lot. Through the research I have done under the guidance of Professor Charles Smith, I have learned several new programming languages, I have been introduced to structure functions and turbulence theory, I have had the opportunity to present my work at professional conferences around the country, and when I leave New Hampshire for graduate school I will have written at least one and possibly three papers for publication in professional refereed journals. In Chapter 1 of this thesis I outlined and explained some of the basic properties of the sun and the solar wind. Chapter 2 is an extension of these properties to a subdiscipline of solar wind studies that is concerned with the turbulent properties of the solar wind. One of the topics discussed in this chapter is the observed departure of the solar wind temperature as a function of heliocentric distance from the temperature predicted by an adiabatic expansion. This nonadiabatic expansion implies the presence of a heating source in the solar wind. Models based on the turbulent transport of energy provide a sufficient amount of energy to account for the observed heating of the solar wind. This model shows that turbulence is the source of heating in the solar wind. Chapter 3 presented a model of magnetohydrodynamic turbulence that I follow as an explanation of the turbulence in the solar wind. Energy is generated at large scales, it then cascades through the energy-conserving intermediate scales of the inertial range and is eventually dissipated as heat in the small scales of the dissipation range. Chapter 4 took a closer look at the inertial range and in particular examined the energy cascade rate inferred from power spectra and the cascade rate calculated with the third-order structure function of magnetohydrodynamic fluctuations. We show that the cascade rate produced by the power spectral methods are too high. They are so high that they imply the solar wind heats up as it expands from 1 AU. The heating rate computed from the third-order structure function provides a more reasonable estimate of energy cascade. Chapter 5 uses the high frequency end of the inertial range to analyze the spatial evolution of the magnetic variance and wave vector anisotropies. We find solar wind turbulence measured by these two quantities to be nearly identical at 0.3 and 1 AU. The implication of these results is that the turbulence of the solar wind is fully evolved by the time it reaches 0.3 AU.

Bibliography

- [1] Alfvén, H., Existence of electromagnetic-hydrodynamic waves, *Nature*, *150*, 405-406, 1942.
- [2] Balogh, A., Solar Wind: Ulysses, in *Encyclopedia of Astronomy and Astrophysics*, 2006.
- [3] Bavassano, B., M. Dobrowolny, G. Fanfoni, F. Mariani, and N. F. Ness, Radial evolution of power spectra of interplanetary Alfvénic turbulence, *J. Geophys. Res.*, *87*, 3617–3622, 1982.
- [4] Belcher, J. W., L. Davis, and E. J. Smith, Large-amplitude Alfvén waves in the interplanetary medium: Mariner 5, *J. Geophys. Res.*, *74*, 2302–2308, 1969.
- [5] Belcher, J. W. and L. Davis, Large-amplitude Alfvén waves in the interplanetary medium, *J. Geophys. Res.*, *76*, 3534–3563, 1971.
- [6] Bieber, J. W., W. Wanner, and W. H. Matthaeus, Dominant two-dimensional solar wind turbulence with implications for cosmic ray transport, *J. Geophys. Res.*, *101*, 2511–2522, 1996.
- [7] Biermann, L., Kometenschweife und solare Korpuskularstrahlung, *Z. Astrophys.*, *29*, 1951.
- [8] Blackman, R. B., and J. W. Tukey, *The Measurement of Power Spectra*, Dover, Mineola, N. Y., 1958.
- [9] Burlaga, L. F., Solar wind: Magnetic field, *Encyclopedia of Astronomy and Astrophysics*, 2006.
- [10] Burlaga, L. F., N. F. Ness, A. H. Acuña, R. P. Lepping, J. E. P. Connerney, E. C. Stone, Crossing the termination shock into the heliosheath: Magnetic fields, *Science*, *309* 2027–2029, 2005.
- [11] Chapman, S., Note on the solar corona and the terrestrial ionosphere, *Smithsonian Centr. Astrophys.*, *2* 1957.
- [12] Cranmer, S. R., Why is the fast solar wind fast and the slow solar wind slow?, *Solar Wind 11 - SOHO 16 Conference Proceedings*, 2005.
- [13] Dasso, S., L. J. Milano, W. H. Matthaeus, and C. W. Smith, Anisotropy in Fast and Slow Solar Wind Fluctuations, *Astrophys. J. Lett.*, *635*, L181–L184, 2005.
- [14] Elsässer, W. M., The hydromagnetic equations, *Phys. Rev.*, *79*, 183, 1950.

- [15] European Space Agency and the National Aeronautics and Space Administration, SOHO, [Online], 30 June, 2003. <http://sohowww.nascom.nasa.gov>.
- [16] Feimer, W., Voyager at 90 AU, National Aeronautics and Space Administration, November 20, 2003.
- [17] Fowles, G. R., and G. L. Cassiday, *Analytical Mechanics*, Belmont, CA: Thomson Brooks/Cole, 2005.
- [18] Freeman, J. W., Estimates of solar wind heating inside 0.3 AU. *Geophys. Res. Lett.*, *15*, 88–91, 1988.
- [19] Ghosh, S., W. H. Matthaeus, D. A. Roberts, and M. L. Goldstein, The evolution of slab fluctuations in the presence of pressure-balanced magnetic structures and velocity shears, *J. Geophys. Res.*, *103*, 23,691–23,704, 1998a.
- [20] Ghosh, S., W. H. Matthaeus, D. A. Roberts, and M. L. Goldstein, Waves, structures, and the appearance of two-component turbulence in the solar wind, *J. Geophys. Res.*, *103*, 23,705–23,715, 1998b.
- [21] Gurnett, D. A., Solar Wind Plasma Waves, *Encyclopedia of Astronomy and Astrophysics*, 2006.
- [22] Hamilton, K., C. W. Smith, B. J. Vasquez, and R. J. Leamon, *J. Geophys. Res.*, submitted, 2007.
- [23] Hundhausen, A. J., *Coronal Expansion and Solar Wind*, Berlin, Germany: Springer, 1972.
- [24] Isenberg, P. A., C. W. Smith, and W. H. Matthaeus, Turbulent heating of the distant solar wind by interstellar pickup protons,” *Astrophys. J.*, *592*, 564–573, 2003.
- [25] Jet Propulsion Laboratory, Ulysses:Mission Overview, [Online], 30 January, 2003. <http://ulysses.jpl.nasa.gov>.
- [26] Jet Propulsion Laboratory, Voyager Mission, [Online], 25 August, 2005. <http://voyager.jpl.nasa.gov>.
- [27] Krieger, A. S., A. F. Timothy, and E. C. Roelof, A coronal hole and its identification as the source of a high velocity solar wind stream, *Solar Phys.*, *29*, 505, 1973.
- [28] Kolmogorov, A. N., The local structure of turbulence in incompressible viscous fluid for very large Reynolds numbers, *Dokl. Akad. Nauk SSSR*, *30*, 301–305, 1941a. (Reprinted in *Proc. R. Soc. London A*, *434*, 9–13, 1991.)
- [29] Kolmogorov, A. N., Energy dissipation in locally isotropic turbulence, *Dokl. Akad. Nauk SSSR*, *32*, 16–18, 1941b. (Reprinted in *Proc. R. Soc. London A*, *434*, 15–17, 1991.)
- [30] Kraichnan, R. H., Inertial range of hydromagnetic turbulence, *Phys. Fluids*, *8*, 1385–1387, 1965.

- [31] Leamon, R. J., C. W. Smith, N. F. Ness, W. H. Matthaeus, and H. K. Wong, Observational constraints on the dynamics of the interplanetary magnetic field dissipation range, *J. Geophys. Res.*, *103*, 4775–4787, 1998.
- [32] Leamon, R. J., C. W. Smith, N. F. Ness, and H. K. Wong, Dissipation range dynamics: Kinetic Alfvén waves and the importance of β_e , *J. Geophys. Res.*, *104*, 22,331–22,344, 1999.
- [33] Marsch, E., Kinetic Physics of the Solar Wind Plasma, in *Physics of the Inner Heliosphere, vol. 2*, edited by R. Schwenn and E. Marsch, p. 45–122, Springer-Verlag, Berlin, 1991.
- [34] Marsch, E., Turbulence in the solar wind, in *Reviews in Modern Astronomy, vol. 4*, edited by G. Klare, p. 145–156, Springer-Verlag, New York, 1991.
- [35] Matthaeus, W. H. and M. L. Goldstein, Stationarity of magnetohydrodynamic fluctuations in the solar wind, *J. Geophys. Res.*, *87*, 10,347–10,354, 1982.
- [36] Matthaeus, W. H., M. L. Goldstein, and J. H. King, *J. Geophys. Res.*, *91*, 59, 1986.
- [37] Matthaeus, W. H. and M. L. Goldstein, Low-frequency $1/f$ noise in the interplanetary magnetic field, *Phys. Rev. Lett.*, *57*, 4,495–498, 1986.
- [38] Matthaeus, W. H. and Y. Zhou, Extended inertial range phenomenology of magnetohydrodynamic turbulence, *Phys. Fluids B*, *1*(9), 1929–1931, 1989.
- [39] Matthaeus, W. H., M. L. Goldstein, and D. A. Roberts, Evidence for the presence of quasi-two-dimensional nearly incompressible fluctuations in the solar wind, *J. Geophys. Res.*, *95*, 20,673–20,683, 1990.
- [40] Matthaeus, W. H., C. W. Smith and S. Oughton, Dynamical age of solar wind turbulence in the outer heliosphere, *J. Geophys. Res.*, *A103*, 6495–6502, 1998.
- [41] Matthaeus, W. H., G. P. Zank, C. W. Smith, and S. Oughton, Turbulence, spatial transport, and heating of the solar wind, *Phys. Rev. Lett.*, *82*, 3,444–3,447, 1999.
- [42] McComas, D. J., S. J. Bame, P. Barker, W. C. Feldman, J. L. Phillips, P. Riley, and J. W. Griffiee, Solar wind electron proton alpha monitor (SWEPAM) for the Advanced Composition Explorer, *Space Science Rev.*, *86* (1-4), 563–612, 1998a.
- [43] McComas, D. J., et. al., Ulysses’ return to the slow solar wind, *Geophys. Res. Lett.*, *25*, 1–4, 1998b.
- [44] Neugebauer, M., and C. W. Snyder, Mariner 2 observations of the solar wind, *J. Geophys. Res.*, *71*, 4469–4484, 1966.
- [45] Parker, E. N., Dynamics of the interplanetary gas and magnetic fields, *Astrophys. J.*, *128* 664–76, 1958.
- [46] Parker, E. N., *Interplanetary Dynamical Processes*, Wiley-Interscience, New York, 1963.
- [47] Parks, G. K., *Physics of Space Plasmas*, Boulder, Colorado: Westview Press, 2004.

- [48] *Plasma Physics of the Local Cosmos*, Washington D.C.: The National Academies Press, 2003.
- [49] Podesta, J. J., D. A. Roberts, and M. L. Goldstein, Power spectrum of small-scale turbulent velocity fluctuations in the solar wind, *J. Geophys. Res.*, *111*, A10109, doi:10.1029/2006JA011834, 2006.
- [50] Politano, H., and A. Pouquet, von Kármán-Howarth equation for magnetohydrodynamics and its consequences on third-order longitudinal structure and correlation functions, *Phys. Rev. E*, **57**(1), R21–R24, 1998a.
- [51] Politano, H., and A. Pouquet, Dynamical length scales for turbulent magnetized flow, *Geophys. Res. Lett.*, *25*, 273–276, 1998b.
- [52] Porsche, H., Helios-mission: Mission objectives, mission verification, selected results, *SSE Conference Proceedings*, 1981.
- [53] Richardson, J. D., K. I. Paularena, A. J. Lazarus, and J. W. Belcher, Radial evolution of the solar wind from IMP 8 to Voyager 2, *Geophys. Res. Lett.*, *22*, 325–328, 1995.
- [54] Roberts, D. A., L. W. Klein, M. L. Goldstein and W. H. Matthaeus, The nature and evolution of magnetohydrodynamic fluctuations in the solar wind: Voyager observations, *J. Geophys. Res.*, *92*, 11,021–11040, 1987.
- [55] Russell, C. T., R. A. Mewaldt, and T. T. von Rosenvinge, *The Advanced Composition Explorer Mission*, Boston: Kluwer Academic Publishers, 1998.
- [56] Schwenn, R., Solar Wind: Global Properties, *Encyclopedia of Astronomy and Astrophysics*, 2006.
- [57] Smith, C. W., W. H. Matthaeus, and N. F. Ness, Measurement of the dissipation range spectrum of magnetic fluctuations in the solar wind with applications to the diffusion of cosmic rays, *Proc. 21st Int. Conf. Cosmic Ray Conf.*, *5*, 280–283, 1990.
- [58] Smith, C. W., M. H. Acuña, L. F. Burlaga, J. L’Heureux, N. F. Ness, and J. Scheifele, The ACE magnetic field experiment, *Space Sci. Rev.*, *86*(1-4), 613–632, 1998.
- [59] Smith, C. W., W. H. Matthaeus, G. P. Zank, N. F. Ness, S. Oughton, and J. D. Richardson, Heating of the low-latitude solar wind by dissipation of turbulent magnetic fluctuations, *J. Geophys. Res.*, *106*, 8253–8272, 2001.
- [60] Smith, C. W., P. A. Isenberg, W. H. Matthaeus, and J. D. Richardson, Turbulent heating of the solar wind by newborn interstellar pickup protons, *Astrophys. J.*, *638*, 508–517, 2006.
- [61] Smith, C. W., B. J. Vasquez, K. Hamilton, Interplanetary magnetic fluctuation anisotropy in the inertial range, *J. Geophys. Res.*, *111*, A09111, doi:10.1029/2006JA011651, 2006b.
- [62] Smith, C. W., K. Hamilton, B. J. Vasquez, and R. J. Leamon, Dependence of the dissipation range spectrum of interplanetary magnetic fluctuations on the rate of energy cascade, *Astrophys. J. Lett.*, *645*, 85–88, 2006.

- [63] Smith, C. W., B. J. Vasquez, K. Hamilton, B. T. MacBride, J. A. Tessein, M. A. Forman, R. J. Leamon, Turbulence spectrum of interplanetary magnetic fluctuations and the rate of energy cascade, IGPP Conference Proceedings, 2007.
- [64] Stone, E. C. The Advanced Composition Explorer, *The Advanced Composition Explorer Mission*, Boston: Kluwer Academic Publishers, 1998.
- [65] Totten, T. L., J. W. Freeman, and S. Arya, An empirical determination of the polytropic index for the free-streaming solar wind using Helios 1 data, *J. Geophys. Res.*, *100*, 13–17, 1995.
- [66] Unti, T. W. J., and M. Neugebauer, Alfvén waves in the solar wind, *Phys. Fluids*, *11*(3), 563–568, 1968.
- [67] Vasquez, B. J., C.W. Smith, K. Hamilton, B. T. MacBride, and R. J. Leamon, Evaluation of the turbulent energy cascade rates from the upper inertial range in the solar wind at 1AU, *J. Geophys. Res.*, in press, 2007.
- [68] Verma, M. K., D. A. Roberts, and M. L. Goldstein, Turbulent heating and temperature evolution in the solar wind, *J. Geophys. Res.*, *100*, 19839–19850, 1995.
- [69] Wilcox, J. M., The interplanetary magnetic field: Solar origin and interplanetary effects, *Space Sci. Rev.*, *8*, 258, 1968.
- [70] Zank, G. P., W. H. Matthaeus, and C. W. Smith, Evolution of turbulent magnetic fluctuation power with heliospheric distance, *J. Geophys. Res.*, *101*, 17,093–17,108, 1996.
- [71] Zhou, Y., and W. H. Matthaeus, Models of inertial range spectra of interplanetary magnetohydrodynamic turbulence, *J. Geophys. Res.*, *95*, 14,881–14,892, 1990.